NASA/TM–2003–206892, Vol. 25

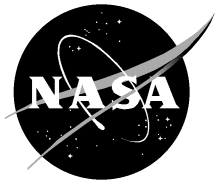

SeaWiFS Postlaunch Technical Report Series

Stanford B. Hooker and Elaine R. Firestone, Editors

Volume 25, Validation of an In-Water, Tower-Shading Correction Scheme

John P. Doyle, Stanford B. Hooker, Giuseppe Zibordi, and Dirk van der Linde

National Aeronautics and
Space Administration

Goddard Space Flight Center
Greenbelt, Maryland 20771

June 2003

The NASA STI Program Office ... in Profile

Since its founding, NASA has been dedicated to the advancement of aeronautics and space science. The NASA Scientific and Technical Information (STI) Program Office plays a key part in helping NASA maintain this important role.

The NASA STI Program Office is operated by Langley Research Center, the lead center for NASA's scientific and technical information. The NASA STI Program Office provides access to the NASA STI Database, the largest collection of aeronautical and space science STI in the world. The Program Office is also NASA's institutional mechanism for disseminating the results of its research and development activities. These results are published by NASA in the NASA STI Report Series, which includes the following report types:

- TECHNICAL PUBLICATION. Reports of completed research or a major significant phase of research that present the results of NASA programs and include extensive data or theoretical analysis. Includes compilations of significant scientific and technical data and information deemed to be of continuing reference value. NASA's counterpart of peer-reviewed formal professional papers but has less stringent limitations on manuscript length and extent of graphic presentations.

- TECHNICAL MEMORANDUM. Scientific and technical findings that are preliminary or of specialized interest, e.g., quick release reports, working papers, and bibliographies that contain minimal annotation. Does not contain extensive analysis.

- CONTRACTOR REPORT. Scientific and technical findings by NASA-sponsored contractors and grantees.

- CONFERENCE PUBLICATION. Collected papers from scientific and technical conferences, symposia, seminars, or other meetings sponsored or cosponsored by NASA.

- SPECIAL PUBLICATION. Scientific, technical, or historical information from NASA programs, projects, and mission, often concerned with subjects having substantial public interest.

- TECHNICAL TRANSLATION. English-language translations of foreign scientific and technical material pertinent to NASA's mission.

Specialized services that complement the STI Program Office's diverse offerings include creating custom thesauri, building customized databases, organizing and publishing research results... even providing videos.

For more information about the NASA STI Program Office, see the following:

- Access the NASA SIT Program Home Page at http://www.sti.nasa.gov/STI-homepage.html

- E-mail your question via the Internet to help@sti.nasa.gov

- Fax your question to the NASA Access Help Desk at (301) 621-0134

- Write to:
  NASA Access Help Desk
  NASA Center for Aerospace Information
  7121 Standard Drive
  Hanover, MD 21076-1320

NASA/TM–2003–206892, Vol. 25

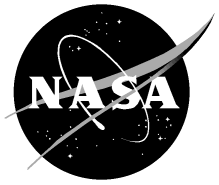

SeaWiFS Postlaunch Technical Report Series

Stanford B. Hooker, Editor
NASA Goddard Space Flight Center, Greenbelt, Maryland

Elaine R. Firestone, Senior Scientific Technical Editor
Science Applications International Corporation, Beltsville, Maryland

Volume 25, Validation of an In-Water, Tower-Shading Correction Scheme

John P. Doyle
JRC/Space Applications Institute, Ispra, Italy

Stanford B. Hooker
NASA Goddard Space Flight Center, Greenbelt, Maryland

Giuseppe Zibordi and Dirk van der Linde
JRC/Institute for Environment and Sustainability, Ispra, Italy

June 2003

ISSN 1522-8789

Available from:

NASA Center for AeroSpace Information
7121 Standard Drive
Hanover, MD 21076–1320
Price Code: A17

National Technical Information Service
5285 Port Royal Road
Springfield, VA 22161
Price Code: A10

Preface

Ocean platforms have a number of advantages over ships and buoys as ocean color data collection platforms, e.g., they are common in coastal regions, stable, frequently equipped with ample power, manned or frequently visited, and low cost (maintained for other purposes). During the Coastal Zone Color Scanner (CZCS) program, optical data was collected from the *Acqua Alta* Oceanographic Tower (AAOT) for algorithm development. At the time, the influence of a large structure on radiometric measurements, particularly ocean reflectance observations, had not been rigorously addressed and has cast doubt on the accuracy of such measurements. This is particularly important given the 5% water-leaving radiometric accuracy goal for satellite ocean color measurements.

The SeaWiFS Project has been collaborating with researchers from the Joint Research Centre (JRC) on measurement protocols and instrumentation development using the AAOT for several years, and the collaboration has achieved many very important results. One particularly impressive result has been the recent demonstration that an automated above-water reflectance system can provide very high quality data over an extended period of time. This accomplishment can only be exploited if an accurate accounting of platform perturbation effects is available. The work documented in this report summarizes the modeling and *in situ* data collection and analysis approach that was undertaken to establish the areal extent of the perturbation and the associated correction. As a result, an initial methodology that can be applied to other platforms is now available. Ultimately, this may allow for a much more extensive, and cost-effective network of coastal validation sites.

Greenbelt, Maryland — C. R. McClain
April 2003

Table of Contents

Prologue 1
1. *In Situ* Sampling Equipment and Methods 3
1.1 Introduction 3
1.2 The AAOT 4
1.3 *In Situ* Instruments 4
1.3.1 AOP Instruments 4
1.3.2 IOP Instruments 6
1.4 *In Situ* Methods 6
1.4.1 AOP Methods 6
1.4.2 IOP Methods 6
2. The Long Distance Deployment System (LDDS) 8
2.1 Introduction 8
2.2 The LDDS 8
2.2.1 The Multiple-Distance Configuration 9
2.2.2 The Single-Distance Configuration 9
3. Theoretical and *In Situ* Data Analysis Methods 11
3.1 Introduction 11
3.2 Theoretical Methods 11
3.2.1 Model Principles 11
3.2.2 Shading Effects 12
3.3 *In Situ* Methods 12
3.3.1 Optical Data Processing 12
3.3.2 Experimental Uncertainties 14
3.4 Summary 16
4. Preliminary Results 17
4.1 Introduction 17
4.2 AAOT Site Conditions 24
4.2.1 Experiment 6 25
4.2.2 Experiment 16 25
4.2.3 Experiment 18 26
4.3 Data Comparisons 26
4.4 Conclusions 27
Acknowledgments 28
Appendix A 28
Appendix B 28
Appendix C 29
Glossary 29
Symbols 29
References 30
The SeaWiFS Postlaunch Technical Report Series 31

Abstract

Large offshore structures used for the deployment of optical instruments can significantly perturb the intensity of the light field surrounding the optical measurement point, where different portions of the visible spectrum are subject to different shadowing effects. These effects degrade the quality of the acquired optical data and can reduce the accuracy of several derived quantities, such as those obtained by applying bio-optical algorithms directly to the shadow-perturbed data. As a result, optical remote sensing calibration and validation studies can be impaired if shadowing artifacts are not fully accounted for. In this work, the general in-water shadowing problem is examined for a particular case study. Backward Monte Carlo (MC) radiative transfer computations—performed in a vertically stratified, horizontally inhomogeneous, and realistic ocean–atmosphere system—are shown to accurately simulate the shadow-induced relative percent errors affecting the radiance and irradiance data profiles acquired close to an oceanographic tower. Multiparameter optical data processing has provided adequate representation of experimental uncertainties allowing consistent comparison with simulations. The more detailed simulations at the subsurface depth appear to be essentially equivalent to those obtained assuming a simplified ocean–atmosphere system, except in highly stratified waters. MC computations performed in the simplified system can be assumed, therefore, to accurately simulate the optical measurements conducted under more complex sampling conditions (i.e., within waters presenting moderate stratification at most). A previously reported correction scheme, based on the simplified MC simulations, and developed for subsurface shadow-removal processing of in-water optical data taken close to the investigated oceanographic tower, is then validated adequately under most experimental conditions. It appears feasible to generalize the present tower-specific approach to solve other optical sensor shadowing problems pertaining to differently shaped deployment platforms, and also including surrounding structures and instrument casings.

Prologue

A primary requirement for in-water optical data measurement activities is to minimize any perturbations negatively influencing the accuracy of the observations. This is particularly true when the data are used as references or *sea truth* for vicarious calibration or algorithm validation of remotely sensed ocean color data (and derived biogeochemical products). The *in situ* optical data accuracy must be defined with respect to the radiometric uncertainty budget, e.g., aimed at complying with the 5% radiometric accuracy of the Sea-viewing Wide Field-of-view Sensor (SeaWiFS) instrument data (Hooker and McClain 2000).

Radiometric accuracy objectives can only be achieved if all the optically perturbing factors are minimized, or accounted for, so they provide an intrinsic, or corrected, radiometric uncertainty that cumulatively does not exceed the prescribed accuracy limit. Under linear perturbation hypotheses, each perturbation factor must be analyzed independently to establish its magnitude and relative importance to the total uncertainty budget. The analyses presented here only address perturbations originating from optical sensor shadowing, and emphasis is placed on the perturbation contribution brought by the instrument deployment structure, in this case an offshore oceanographic tower.

The shadowing perturbations influencing optical measurements of the in-water radiant energy field, and induced by the instrument deployment structure or by the instrument casing itself, can be quantified using three-dimensional (3-D) backward Monte Carlo (MC) simulation techniques (Gordon 1985). The measured light field intensity and directional properties are different from those existing within an unperturbed ocean–atmosphere system, because of the localized modification of optical propagation in the vicinity of the in-water instrument and the deployment platform. The local modification is a function of the spectral opacity and reflectivity, plus the finite 3-D shape, extension, and location of the intervening shadowing structures with respect to the radiation source (the sun) and the instrument detectors.

The accuracy of results generated by bio-optical algorithms, which provide biological and physical parameters of the investigated water body as a function of the *in situ* light field, is degraded by unaccounted for shadowing artifacts. These can ultimately impair the quality of ocean color calibration and validation activities. Such negative effects must be minimized wherever possible. For the instrument self-shading problem, optical data correction schemes can be based on analytical methods, as formulated by Gordon and Ding (1992) and experimentally validated by Zibordi and Ferrari (1995). When complex shadowing by large and irregular deployment structures must be addressed, a viable approach is customized look-up tables or comprehensively detailed and quasi-real time MC simulations, as proposed by Doyle and Zibordi (2002) for a specific oceanographic tower case.

In an initial study, Zibordi et al. (1999) considered three aspects of the platform perturbation problem:

- The empirical quantification of tower-shading effects through a first set of shadowing experiments,
- An initial evaluation of the MC simulation capabilities and accuracy, and
- An assessment of the correction scheme guidelines and development effort.

Results from the initial inquiry showed that under ordinary conditions, tower-shading can reduce the absolute in-water radiometric values by about 1–10%, thus substantially exceeding the allowed uncertainty in radiometric data used for SeaWiFS calibration and validation activities. More recent work (Doyle and Zibordi 2002) illustrated the applied backward MC simulation techniques, the theoretical 3-D validation exercises, the oceanographic tower site and atmosphere–ocean system modeling characteristics, as well as the principles and theoretical results achieved with the look-up table shadowing-correction scheme.

In the investigation presented here, the *in situ* validation of the proposed correction scheme is attempted by elaborating on the findings from a second, more dedicated, and extensive field campaign. The shadowing experiments were carefully planned to conduct accurate and spatially controlled radiance and irradiance measurements of the in-water light field existing in close proximity of the *Acqua Alta* Oceanographic Tower (AAOT), located in the northern Adriatic Sea and used regularly as an ocean color calibration and validation site as part of the Coastal Atmosphere and Sea Time-Series (CoASTS) project. The second campaign took place from 5–17 July 1998, with the sequential day of the year (SDY) covering days 186–198. The science team members for investigating in-water tower perturbations are presented in Appendix A.

1. *In Situ Sampling Equipment and Methods*

The *in situ* sampling equipment used during the tower-shading campaigns was a combination of the instruments normally used in the ocean color activities performed at the tower and those needed for the specialized experiments associated with quantifying in-water tower perturbations. The former includes a large diversity of marine and atmospheric measurements for the calibration and validation of ocean color remote sensors, while the latter includes a new in-water optical system with a specialized positioning capability. Tower deployments have also been used as an opportunity to evaluate new instruments designed for the special circumstances associated with the coastal environment. Within this objective, the tower-shading experiments were used to begin a preliminary evaluation of a new in-water profiler.

2. *The Long Distance Deployment System (LDDS)*

The LDDS was designed to facilitate the deployment of free-falling optical profilers relatively far from the AAOT. It consists primarily of a black plastic-covered stainless steel cable with one end anchored to the sea floor and the other end secured to the top-most deck of the AAOT. The LDDS can be operated in a multiple-distance or single-distance configuration. The multiple-distance configuration ensures accurate and quick deployment of the free-falling profiler from 1–35 m from the AAOT in 1 m incremental steps. This configuration was used to investigate the tower perturbations on in-water optical data. The single-distance configuration permits the deployment of a free-falling profiler at an arbitrary distance from the tower (within a maximum distance of about 35 m), although, it is usually used at a fixed distance of 28 m (i.e., well beyond the influence of perturbations associated with the tower). This latter configuration is used during the CoASTS measurement campaigns for the operational deployment of the miniature NASA Environmental Sampling System (mini-NESS) profiler. The semirigid frame created by the taut steel cable, significantly improved the capability for controlling the starting location of the deployment and the descent of the profiler. Departures from an ideal vertical cast occurred only during strong currents.

3. *Theoretical and In Situ Data Analysis Methods*

The comparison of theoretical and *in situ* AAOT perturbed radiometric data, was carried out using MC simulations and optical profiles collected at incremental distances from the tower superstructure. In both cases, the AAOT shading effects on radiometric data were quantified with respect to far-field data (assumed unperturbed). The backward MC simulations of the atmosphere–ocean–AAOT–detector system accounted for the marine and atmospheric inherent optical properties (IOPs), the seawater vertical stratification, the AAOT geometry, and the sensor field of view. The determination of the tower perturbations from the optical profiles required the creation of quality assured fixed-depth optical cross sections. These were then fitted with a multiparameter function to minimize noise perturbations affecting single distance measurements. Confidence bands were also produced for each fitted function to provide error bars suitable for the comparison with the theoretical data.

4. *Preliminary Results*

The measurements from three field experiments, collected under very different environmental conditions, compare well with simulated model data. Under extreme conditions, however, high uncertainties in the estimated results are produced by excessive instrument tilt and by wave-focusing effects. Shadowing perturbations for very clear waters are restricted to within 15–20 m from the tower legs for upwelling radiance and downward irradiance. The far-field unperturbed distance is reached at 20–25 m in relatively turbid waters. Under overcast conditions, the magnitude of the shadowing effect is larger than under clear sky conditions and the far-field distance is reached at approximately 30 m from the tower legs.

Chapter 1

In Situ Sampling Equipment and Methods

Stanford B. Hooker
NASA/Goddard Space Flight Center
Greenbelt, Maryland

Giuseppe Zibordi
JRC/Institute for Environment and Sustainability
Ispra, Italy

Abstract

The *in situ* sampling equipment used during the tower-shading campaigns was a combination of the instruments normally used in the ocean color activities performed at the tower and those needed for the specialized experiments associated with quantifying in-water tower perturbations. The former includes a large diversity of marine and atmospheric measurements for the calibration and validation of ocean color remote sensors, while the latter includes a new in-water optical system with a specialized positioning capability. Tower deployments have also been used as an opportunity to evaluate new instruments designed for the special circumstances associated with the coastal environment. Within this objective, the tower-shading experiments were used to begin a preliminary evaluation of a new in-water profiler.

1.1 INTRODUCTION

The sampling equipment used for the second tower-shading campaign was a refinement of the instrumentation deployed during the first campaign (Zibordi et al. 1999). The improvements to the second field campaign were as follows:

1. Use of a smaller and lighter in-water optical system for making profiles at a variable distance from the tower, and
2. Use a more rigid and accurate deployment system for placing the optical system at the desired distance from the tower.

The new deployment system was also easier to operate, which allowed for more measurements to be made within a shorter period of time.

The profiler that was used to measure the in-water light field at varying distances from the AAOT during the first tower-shading campaign was the Low Cost NASA Environmental Sampling System (LoCNESS). This profiler was built from off-the-shelf modular components and was designed to be a low-cost alternative to the expensive, integrated free-fall instruments at the time (Aiken et al. 1998). Although LoCNESS was a very capable profiler in the deep ocean (Hooker and Maritorena 2000), it was difficult to use in the shallow water in the vicinity of the AAOT. Consequently, the SeaWiFS Field Team worked with the manufacturer of LoCNESS, Satlantic, Inc. (Halifax, Canada), to produce a more compact version of the LoCNESS instrument.

The smaller profiler differed from the previous larger one by positioning both of the light sensors at the end or *tail* of the profiler, but opposite to one another on the fins. The significant advantage of this design is it places the two sensors in very nearly the same horizontal plane, which is a more appropriate configuration for coastal waters, wherein vertical complexity (usually arising from optically differing thin layers) is a recurring feature of the water column. This new layout also reduced the risk of possible sensor damage from an impact with the sea floor.

For the first tower-shading campaign, the experimental setup began with siting a black buoy approximately 30 m from the southern tower leg. The buoy was aligned perpendicularly to the southeastern side of the tower and displaced approximately 2 m to the side of the Wire-Stabilized Profiling Environmental Radiometer (WiSPER) instrument. Two pulleys were then attached—one to the buoy and the other to tower—and a closed loop of line (60 m long) with marks on it every 2.5 m was run through the pulleys. A cable ring was linked to one of the cable marks, which defined the current position of the profiler (the power

and telemetry cable for the profiler passed through the ring). The ring and, thus, the profiler, was moved to a selected distance from the tower leg by pulling on the closed loop of line, until the desired number of cable marks between the position of the ring and the tower leg was achieved.

Although this simplistic positioning system permitted a reliable positioning of the optical system, it was not sufficiently rigid (and, thus, accurate) for repeated use over extended time periods. The continued deployment of a small profiler at a fixed or variable far-field distance was a desired capability during CoASTS campaigns, so a new system was designed and deployed at the AAOT. This new system is described in Chapt. 2.

1.2 THE AAOT

The AAOT is located in the northern Adriatic Sea (12.51°E,45.31°N) approximately 15 km southeast of the city of Venice. The average water depth immediately below the tower is 17.5 m and the composition of the nearby sea floor is primarily sand and silt. The tower was built in 1970 and is owned and operated by the *Istituto per lo Studio della Dinamica delle Grandi Masse* (ISDGM) of the Italian *Consiglio Nazionale delle Ricerche*† (CNR), in Venice.

The tower is composed of four levels supported by four large pillars. Each level is approximately $7.2\times5.2\,m^2$ in size with the exception of the lowest level, which is $5.2\times5.2\,m^2$. Detailed descriptions of the AAOT and its use for optical field measurements are presented in Hooker et al. (1999) and Zibordi et al. (2002).

1.3 *IN SITU* INSTRUMENTS

The principal *in situ* instruments that were deployed to directly support the data analysis for the second tower-shading campaign were designed to measure the IOPs and apparent optical properties (AOPs) of seawater. A variety of other instruments, which helped characterize the biogeochemical and meteorological properties of the environment during optical data collection, were also used where necessary. Although the majority of the data were collected as continuous data sequences, either vertically or temporally, discrete water samples were collected for laboratory analysis.

1.3.1 AOP Instruments

The miniNESS and WiSPER profilers used 7-channel ocean color radiance series-200 (OCR-200) sensors, as well as 7-channel ocean color irradiance series-200 (OCI-200) sensors. Both systems used a 16-bit analog-to-digital (A/D) data converter unit, the so-called DATA-100, and acquired data at 6 Hz. All these instruments were built by Satlantic, Inc. (Halifax, Canada).

Both of the in-water systems provided profiles of upwelling radiance $L_u(z,\lambda)$ and downward irradiance $E_d(z,\lambda)$ in seven spectral bands. In addition, the WiSPER E_d sensor was rotated 180° to measure the upward irradiance, $E_u(z,\lambda)$. The latter data were collected in between two sequential E_d profiles.

An additional OCI-200 was used to measure the above-water (solar) downward irradiance $E_d(0^+,\lambda)$. The solar reference data were acquired simultaneously with the in-water profiles and were required to a) correct the in-water measurements for changes in the illumination conditions during casts, and b) derive normalized quantities, like the remote sensing reflectance, $R_{rs}(\lambda)$.

The center wavelengths, λ, of the optical radiometers were closely matching the nominal center wavelengths of most of the SeaWiFS instrument channels: 412, 443, 490, 510, 555, 665, and 683 nm; actual center wavelengths were within 1 nm of these values. A comparison of the actual center wavelengths for miniNESS and WiSPER is presented in Table 1.

Table 1. Channel numbers and center wavelengths (in nanometers) for the radiometric sampling systems. The sensor systems are given with their individual sensor codes, which are formed from a one-letter designator for the type of sensor, plus a three-digit serial number (S/N). The solar reference, M099, is shown only once, but it was used with both profilers. All of the channels have 10 nm bandwidths.

Channel	*miniNESS*			*WiSPER*	
	R035	I040	M099	R046	I071
1	411.1	411.5	411.5	412.3	411.3
2	442.9	442.5	442.8	442.8	442.9
3	489.9	489.3	489.9	490.5	490.2
4	509.7	509.6	510.3	510.8	510.1
5	554.8	555.4	554.5	554.9	554.8
6	665.0	665.7	664.8	665.8	665.6
7	683.1	683.2	683.2	683.9	683.6

A solar occulter was used to periodically shade the direct sun irradiance during $E_d(0^+,\lambda)$ measurements to provide diffuse irradiance data, $E_i(0^+,\lambda)$. The latter were used to determine the ratio of the diffuse to direct downward irradiance, r_d, which is needed in the formulations to correct for instrument self-shading and AAOT perturbation effects in the underwater optical measurements.

The absolute calibration of the miniNESS and WiSPER radiometers was made just before and after the field measurements. An analysis of the computed calibration coefficients showed variations to within 1.5%.

† The Institute for the Study of Large Masses of the Italian National Research Council.

1.3.1.1 miniNESS

The miniNESS profiler is a rocket-shaped device with a weighted nose and buoyant (foam) fins affixed to a tail bracket. The free-fall aspects of the LoCNESS and miniNESS designs were derived from the SeaWiFS Free-Falling Advanced Light Level Sensors (SeaFALLS) profiler. The SeaFALLS profiler was a modified version of the Satlantic SeaWiFS Profiling Multichannel Radiometer (SPMR). The primary modification was to increase the so-called *righting moment*, which is the tendency of the nose of the profiler to swing downwards once the rocket is released, by adding larger fins and increasing the amount of weight attached to the nose. The larger fins have an increased surface area, which improves the stability of the rocket as it falls through the water column.

The primary difference between miniNESS and other free-fall profilers is the light sensors are mounted on the fins (Fig. 1), rather than at the ends of the instrument centerline. Fin mounts allow the light sensors to be very nearly placed in the same horizontal plane, which is an important capability in waters with a complicated vertical structure, e.g., coastal waters.

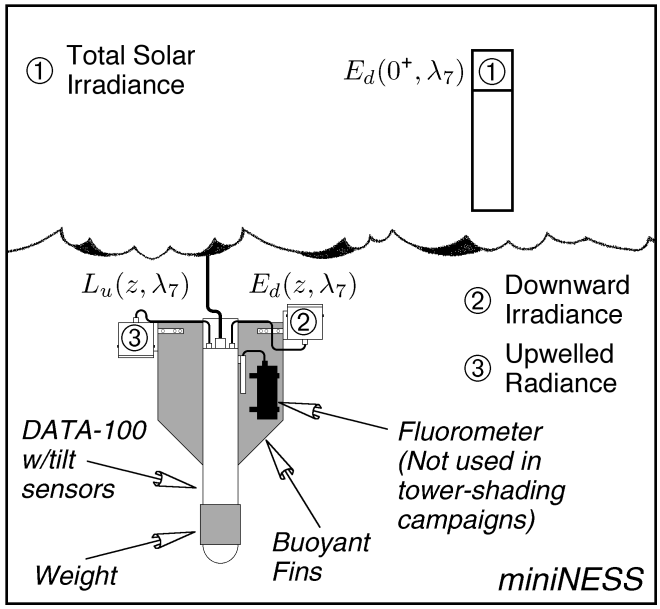

Fig. 1. A schematic of the miniNESS profiler.

The first miniNESS profiler was deployed in the deep ocean during a cruise from South Africa to England from 15 May to 16 June 1998, and then again during a cruise from England to the Falkland Islands from 11 September to 17 October 1998, that is, immediately before and after the second tower-shading campaign. The primary reason for deploying miniNESS on these deep ocean cruises was to compare its performance against established free-fall profilers under a variety of environmental conditions.

A comparison of miniNESS with simultaneous deployments of LoCNESS and SeaFALLS is presented in Fig. 2. Although the data are well distributed with respect to the 1:1 line, there is a noticeable bias in the 510 nm data. The average (over the number of simultaneous casts) unbiased percent difference (UPD)† between the two data sets for each channel ranges from −0.4 to +10.8% for the 443 and 510 nm wavelengths, respectively. If the 510 nm channel is ignored, the spectrally averaged UPD value is −2.4%, which is to within calibration uncertainties for radiance sensors (Hooker et a. 2002).

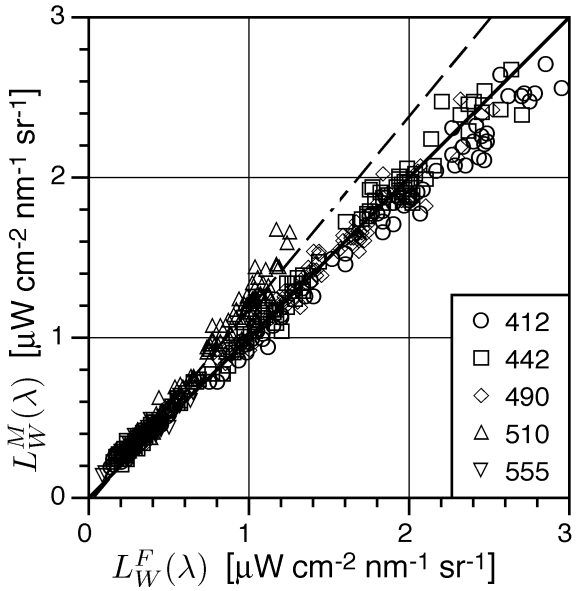

Fig. 2. A comparison of water-leaving radiances derived from miniNESS, $L_W^M(\lambda)$, versus those from traditional free-fall profilers, $L_W^F(\lambda)$, i.e., LoCNESS and SeaFALLS. The dashed line is a linear fit for the 510 nm channel.

Difficulties with the 510 nm channels have been documented in other intercomparisons of Satlantic profilers (Hooker and Maritorena 2000), but no justification for the differences has ever been documented. These types of problems are a reminder of the continuing need to intercompare instruments and calibration procedures if uncertainties are to be controlled.

1.3.1.2 WiSPER

WiSPER is a winched system deployed through a custom-built profiling rig with the optical sensors mounted at approximately the same depth and distance (i.e., within a 10 cm relative depth, and 80 cm relative distance) and deployed at 7.5 m from the main structure of the AAOT. The winch speed is approximately 0.1 m s^{-1}, which, when combined with the 6 Hz data acquisition rate of the optical sensors, provides 64 measurements per meter. The rigidity and stability of the rig is maintained through two

† The unbiased percent difference, $\bar{\psi}$, between two quantities X and Y is defined as $\bar{\psi} = 200(X - Y)/(X + Y)$.

taut wires, anchored between the tower and a weight on the sea bottom, which prevents the movement of the rig out of the vertical plane of the wires (Fig. 3). The wire stabilization and the relatively low deployment speed ensures a good characterization of the subsurface water layer, thereby minimizing the extrapolation uncertainties in determining subsurface radiance and irradiance values.

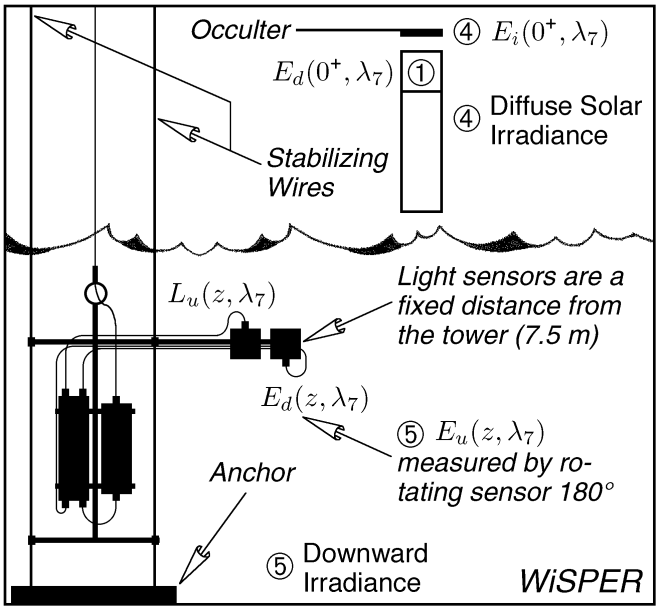

Fig. 3. A schematic of the WiSPER profiler.

1.3.2 IOP Instruments

The aforementioned complexity of the coastal water column can add a substantial difficulty in deriving surface quantities from underwater AOP measurements. The presence of one or more optically different thin layers can alter the usual log-transformed linear decay of the measured near-surface optical properties, and, thus, significantly degrade the accuracy of the (estimated) surface values.

Contemporaneous IOP profiles with the AOP profiles provide a qualitative capability for evaluating whether or not the near-surface layer used for AOP extrapolations includes layers or intrusions that would significantly degrade the ability to use a log-transformed linear fit. Consequently, the WiSPER system includes the simultaneous collection of spectral absorption and attenuation, $a(z, \lambda)$ and $c(z, \lambda)$, respectively, using a Western Environmental Technology Laboratories (WETLabs), Inc. (Philomath, Oregon) 25 cm pathlength AC-9. The nine AC-9 bands are in the 412–715 nm spectral range and are 10 nm wide. A Sea-Bird Electronics (Bellevue, Washington) 5T submersible pump was used to provide a constant water flow through the AC-9.

1.4 *IN SITU* METHODS

The methods used to conduct *in situ* measurements are essentially the same as those described previously in Zibordi et al. (1999) and Hooker et al. (2003) for previous tower experiments. Some methodological details are in order, however, because they are specific to the (in-water) tower-shading campaigns.

1.4.1 AOP Methods

The objective of the field campaign was to estimate the shadowing effects on in-water radiometry as a function of distance from the AAOT structure. Briefly, each experiment consisted of collecting, during less than 15 min of time, a sequence of in-water vertical profiles of downward irradiance $E_d(x, z, \lambda, t)$ and upwelling nadir radiance $L_u(x, z, \lambda, t)$ at varying horizontal distances x from the tower (with x ranging from 2.5–30 m), as a function of depth z, wavelength λ, and acquisition time t. All optical data were recorded making use of OCR-200 and OCI-200 radiometers providing radiance and irradiance readings, respectively.

Sequential optical profiles were taken with the miniNESS free-falling profiler. The miniNESS instrument was positioned at variable distances from the tower legs using the LDDS (Chapt. 2). Concurrent with miniNESS data, incident above-water solar irradiance data, $E_d(0, 0^+, \lambda, t)$, were collected with a Multichannel Visible Detector System (MVDS). The miniNESS deployments were performed from the southern tower leg along the x direction, running northwest to southeast (i.e., along a vertical sampling plane that intersects close to the location where the routine WiSPER in-water optical profiles are performed, at 7.5 m from the tower legs).

1.4.2 IOP Methods

The IOPs used to support the analysis of the optical data collected within the AAOT shadowing experiment were the beam attenuation $c(z, \lambda)$ and absorption $a(z, \lambda)$ coefficients. The coefficients $c(z, \lambda)$ and $a(z, \lambda)$ were computed from calibrated beam attenuation and absorption coefficients, $\hat{c}_{t-w}(z, \lambda)$ and $\hat{a}_{t-w}(z, \lambda)$, respectively, obtained from the AC-9 measurements for suspended and dissolved optical components (not including the contribution of pure seawater). The calibrated coefficients were corrected for salinity and temperature differences between the *in situ* seawater and the pure water used for laboratory calibration, using the conductivity, temperature, and depth (CTD) profile data (WETLabs 2002).

The measured beam attenuation coefficients corrected for salinity and temperature effects do not require any further processing, that is,

$$c(z, \lambda) \;=\; \hat{c}^{ST}_{t-w}(z, \lambda) \;+\; c_w(\lambda), \qquad (1)$$

where the ST superscript denotes the salinity and temperature correction, and $c_w(\lambda)$ is the beam attenuation coefficient for pure water.

The calibrated absorption coefficients need to be further corrected for scattering effects, because the finite acceptance angle of the optics and the incomplete reflectivity of the absorption tube surface prevents the detector from collecting all the scattered light, which induces an overestimate of the retrieved absorption coefficient. In the specific case of the CoASTS campaigns, these perturbation effects were removed using the method proposed by Zaneveld et al. (1994).

The Zaneveld et al. (1994) method is based on the removal of a variable percentage of the scattering coefficient estimated as the difference between $\hat{c}^{ST}_{t-w}(z,\lambda)$ and $\hat{a}^{ST}_{t-w}(z,\lambda)$. The method assumes the absorption coefficient of particulate and dissolved material is zero at a reference wavelength, $\lambda_0 = 715\,\mathrm{nm}$, and the shape of the volume scattering function is independent of wavelength, which means

$$a(z,\lambda) \;=\; \hat{a}^{ST}_{t-w}(z,\lambda) \;+\; a_w(\lambda) \;-\; \breve{a}^{ST}_{t-w}(z,\lambda_0), \qquad (2)$$

where $a_w(\lambda)$ is the absorption of pure water taken from Pope and Fry (1997) and

$$\breve{a}^{ST}_{t-w}(z,\lambda_0) \;=\; \hat{a}^{ST}_{t-w}(z,\lambda_0)\,\frac{\hat{c}^{ST}_{t-w}(z,\lambda) - \hat{a}^{ST}_{t-w}(z,\lambda)}{\hat{c}^{ST}_{t-w}(z,\lambda_0) - \hat{a}^{ST}_{t-w}(z,\lambda_0)}. \qquad (3)$$

Chapter 2

The Long Distance Deployment System (LDDS)

Dirk van der Linde
JRC/Institute for Environment and Sustainability
Ispra, Italy

Abstract

The LDDS was designed to facilitate the deployment of free-falling optical profilers relatively far from the AAOT. It consists primarily of a black plastic-covered stainless steel cable with one end anchored to the sea floor and the other end secured to the top-most deck of the AAOT. The LDDS can be operated in a multiple-distance or single-distance configuration. The multiple-distance configuration ensures accurate and quick deployment of the free-falling profiler from 1–35 m from the AAOT in 1 m incremental steps. This configuration was used to investigate the tower perturbations on in-water optical data. The single-distance configuration permits the deployment of a free-falling profiler at an arbitrary distance from the tower (within a maximum distance of about 35 m), although, it is usually used at a fixed distance of 28 m (i.e., well beyond the influence of perturbations associated with the tower). This latter configuration is used during the CoASTS measurement campaigns for the operational deployment of the miniNESS profiler. The semirigid frame created by the taut steel cable, significantly improved the capability for controlling the starting location of the deployment and the descent of the profiler. Departures from an ideal vertical cast occurred only during strong currents.

2.1 INTRODUCTION

Specialized positioning equipment was designed and used to deploy the miniNESS profiler for the second AAOT shadowing campaign. The objective was to improve the quality of the comparison between *in situ* and theoretical optical data, with respect to the first AAOT tower-shading campaign. The first tower-shading campaign (Zibordi et al. 1999) used a capable, but somewhat simplistic and at times cumbersome, cabling system to move a free-falling profiler to variable distances from the tower in 2.5 m increments. With the original system, it was difficult to move the profiler more than 20 m away from the tower (the maximum distance was 22.5 m), and one of the objectives with the new system was to overcome this limitation, so deployments could take place as far as 30 m away from the tower.

A more accurate radiometer positioning system was developed to conduct in-water profiling experiments in a spatially more controlled and reproducible fashion. The final layout relied strongly on the preparatory efforts undertaken to position, as rigidly as possible, the basic components of the system.

2.2 THE LDDS

A heavy weight with a floating marker buoy was sunk to the sea floor approximately 80 m away from the AAOT southern pillar in the southeast direction. A termination leader with flotation was attached to the anchor before it was deployed. A 10 mm (black) plastic-covered, stainless steel cable with flotation was attached to the floating termination leader and the other end was secured to a manual winch on the top deck of the tower. The steel cable was brought under tension by winching it tightly to the tower (thereby causing the cable flotation on the termination leader and the stainless steel cable to be pulled underwater).

The taut cable extending from the anchor to the top of the tower constitutes the primary mechanical component of the LDDS design. For boating safety, the steel cable cannot be left installed when the platform is not in use. So in addition to the need for rapid installation, the steel cable also needed to be easily dismantled. The latter was accomplished by attaching flotation to the end of the steel cable that was secured to the termination leader. When the tension on the steel cable is released, the end of the steel cable attached to the termination leader floats to the surface. Once on the surface, the steel cable can be detached from the termination leader and recovered on the tower. The flotation on the termination leader keeps the termination point on the surface, so the next installation can proceed quickly.

The variations in how the LDDS is used on the AAOT are determined by the cabling systems that are attached

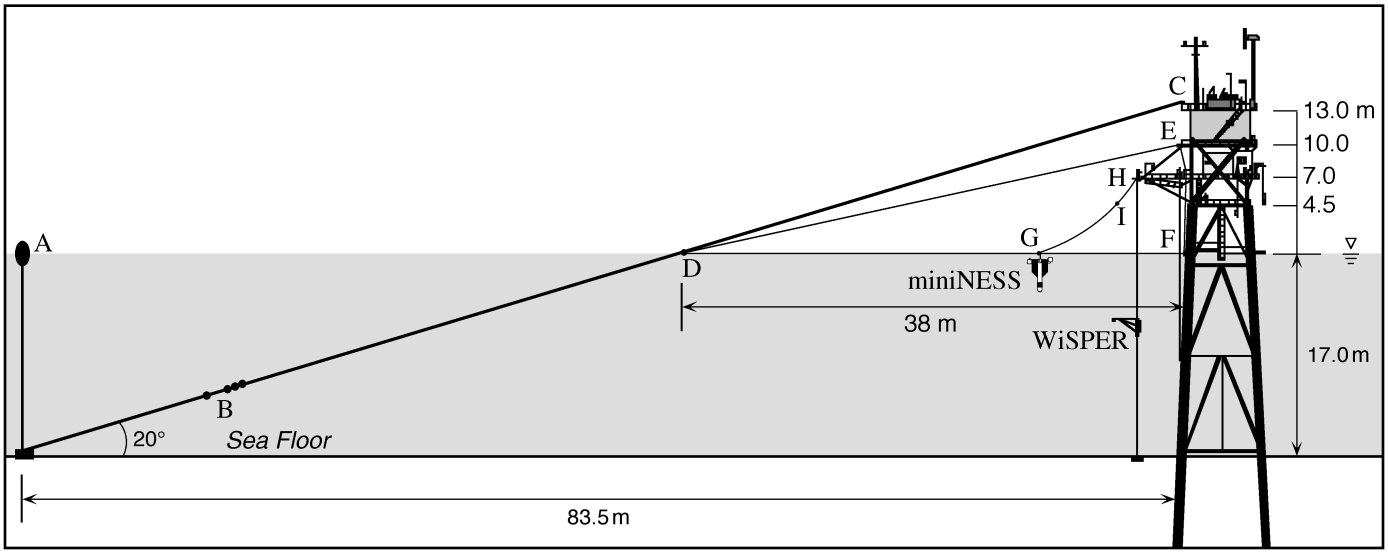

Fig. 4. A schematic of the experimental setup, illustrating the rigid profiling structure for WiSPER, and the taut-wire structure for the multiple-distance configuration of the LDDS for miniNESS. The basic system consists of a surface buoy (point A) attached to a heavy anchor plus a steel cable with one end attached to a termination leader (point B) affixed to the anchor, and the other end attached to a manual winch on the top deck of the tower (point C). The WiSPER system is deployed from a fixed location 7.5 m from the tower, and the miniNESS free-falling profiler is deployed a variable distance from the tower by moving the surfacing ring (point G) along a taut-wire cable extending 38 m from the tower legs as part of a triangular loop of cable (defined by pulleys at points D, E, and F) and operated from the work deck (point H). A cable block (point I) prevents the profiler from descending beyond a predetermined depth (thereby minimizing the risk of a bottom impact).

to the steel cable. The multiple-distance configuration was designed to quickly and accurately change the deployment point of a free falling profiler from the AAOT up to a distance of 35 m in 1 m increments. The single-distance configuration was designed to ensure an easy deployment of a free-falling profiler at a single distance from the AAOT well clear of any perturbative effects associated with the tower (typically about 28 m).

2.2.1 The Multiple-Distance Configuration

For the multiple-distance configuration of the LDDS, an anchorage point and pulley is affixed at the cable–water intersection; this point is located approximately 38 m from the tower base. A second pulley is attached to the AAOT southern pillar about 50 cm from the water surface, and a third pulley is mounted vertically above the second pulley at a height of approximately 10 m. The latter was easily accessible from the third-level railing.

A 6 mm thick black nylon rope is run through the three small pulleys (points D, E, and F in Fig. 4) and brought under tension (which creates a triangular form around the three pulleys). A small floating ring with an inside diameter of 30 mm is attached to the nylon rope along the base of the triangle (point G in Fig. 4). The ring, through which the instrument cable passes, acts as the deployment point. The nylon rope is marked in 1 m increments to accurately identify the deployment distance from the tower.

An operator, standing on the end of the work deck (point H in Fig. 4) closest to the tower, moves the nylon rope (between points E and F in Fig. 4) to bring the floating ring (and the profiler) to the desired distance from the AAOT. When the profiler is at the desired distance, the nylon rope is secured and the profiler is launched by quickly releasing the cable held at the edge of the work deck farthest from the tower. A cable block (point I in Fig. 4) that cannot pass through the cable ring can be used to set the maximum amount of cable that can be released by the operator, and, thus, the maximum depth of the cast. When the maximum depth is reached, the profiler is pulled to the surface at the point from which it was launched.

2.2.2 The Single-Distance Configuration

The single-distance configuration of the LDDS is shown in Fig. 5. It is composed of a pulley block, placed at point E, which includes four small guide wheels rolling over the main cable and a 200 mm diameter pulley guide wheel for the cable of the profiler. There are two small (4 mm) nylon lines on both sides of the pulley system. One is directly laced at point C; the other passes through a small pulley located at point D (also used with the multiple-distance

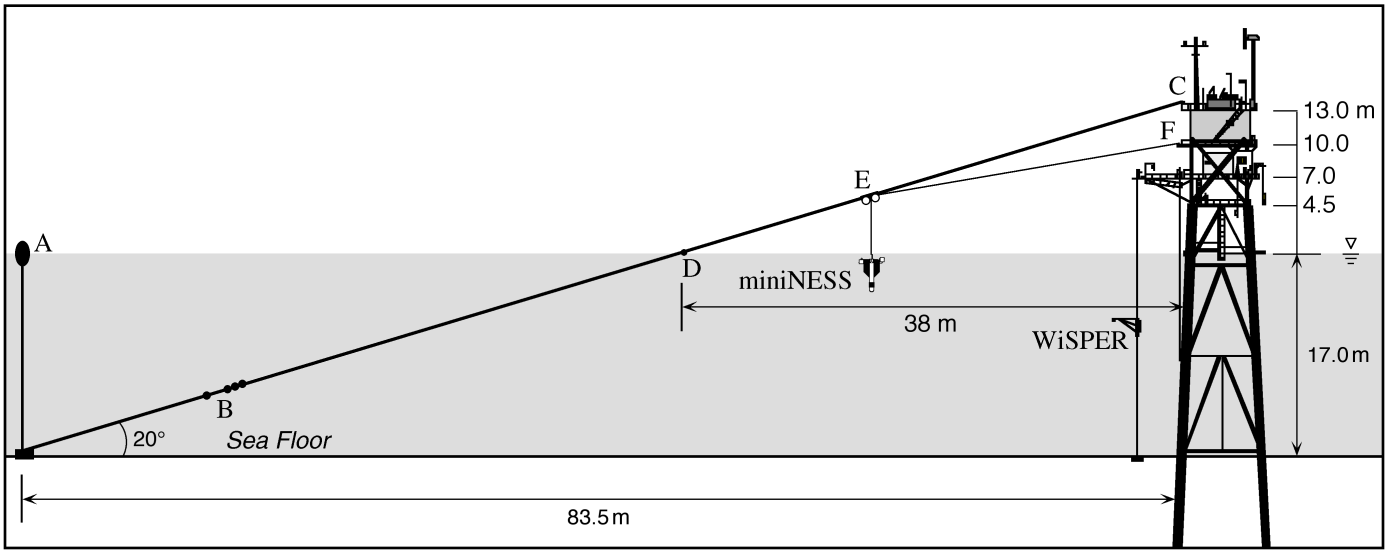

Fig. 5. A schematic of the single-distance configuration of the LDDS for miniNESS. The system consists of the same basic components used in the multiple-distance configuration (Fig. 4): a surface buoy (point A) attached to a heavy anchor, plus a steel cable with one end attached to a termination leader (point B) affixed to the anchor, and the other end attached to a manual winch on the top deck of the tower (point C). The unique component for the single-distance configuration is the pulley block (point E) which is used in concert with two nylon lines run from points E–D–C and E–C to move the pulley block (and, thus, the profiler) along the steel cable (points D–C).

configuration), and is then laced at point C. When the two small nylon lines are used together, it is possible to position the pulley block, and consequently the deployment point E, at any location along the steel cable between points C and D.

The profiler is operated from the middle deck at point F in Fig. 5. In the stand-by position, the profiler is kept about 1 m under the sea surface by blocking the power–telemetry cable on the railing near point F. The maximum deployment depth for the profiler is marked on the cable, and the operator uses this mark to prevent the profiler from sinking too deep and impacting the bottom. The usual deployment distance, indicated by point E, is approximately 28 m from the AAOT.

Chapter 3

Theoretical and *In Situ* Data Analysis Methods

John P. Doyle†
JRC/Space Applications Institute
Ispra, Italy

Abstract

The comparison of theoretical and *in situ* AAOT perturbed radiometric data, was carried out using MC simulations and optical profiles collected at incremental distances from the tower superstructure. In both cases, the AAOT shading effects on radiometric data were quantified with respect to far-field data (assumed unperturbed). The backward MC simulations of the atmosphere–ocean–AAOT–detector system accounted for the marine and atmospheric IOPs, the seawater vertical stratification, the AAOT geometry, and the sensor field of view. The determination of the tower perturbations from the optical profiles required the creation of quality assured fixed-depth optical cross sections. These were then fitted with a multiparameter function to minimize noise perturbations affecting single distance measurements. Confidence bands were also produced for each fitted function to provide error bars suitable for the comparison with the theoretical data.

3.1 INTRODUCTION

The comparison between simulated and experimental data of the AAOT perturbation effects required a) 3-D backward MC modeling of radiance and irradiance data with the specific IOPs and geometry characterizing the AAOT field experiments and b) the implementation of methods for interpreting the optical measurements focusing on the creation of fixed-depth optical cross sections providing an experimental quantification of the AAOT perturbation effects.

3.2 THEORETICAL METHODS

The PHO-TRAN 3-D backward MC code, its variance reduction techniques, and the general atmosphere–ocean–AAOT–detector system are detailed in Doyle and Zibordi (2002). Some details of the simulation system are repeated, because they are novel and specific to the results presented here.

3.2.1 Model Principles

To compare *in situ* with simulated radiometric data, accurate backward MC simulations of radiative transfer processes in the visible and near infrared within a fully 3-D and nonhomogeneous media, were performed on different atmosphere–ocean–AAOT–detector systems closely reproducing those characterizing the tower-shading experiments. These dedicated, realistic systems include four elements:

1. Atmospheric and oceanic IOPs,
2. Vertical stratification of the water column,
3. Detailed AAOT geometry, and
4. The actual sensor field of view together with its light-collecting properties.

One simplification was the spectral reflectivity of the structure was assumed to be zero.

The dedicated MC simulations performed in this study differ from those previously described in Doyle and Zibordi (2002) for the inclusion of the radiometer casings in the modeled system. In this way, the instrument self-shading perturbation affecting the radiometric data were intrinsically simulated by the MC scheme, without the need of applying an analytic self-shading correction (Gordon and Ding 1992). The geometry of the miniNESS main body and its attached buoyancy fins were not included in the simulations, because they were assumed sufficiently small and far from the active sensor to insignificantly perturb the light field at the sensor location.

The radiometer casings are modeled as completely absorbing cylinders (11 cm high and 9 cm in diameter), vertically oriented, and positioned at the required simulation

† Currently with the Imperial College of Science, Technology and Medicine, Computational Physics and Geophysics, London, England.

depth. The detectors are assumed centered on the symmetry axis of the radiometer casing, with point-like collecting areas. The field of view of the radiance sensor was 20° (equivalent to that of the OCI-200 in water).

3.2.2 Shading Effects

In the following analysis, the shading effects are described through the percent relative error (PRE) between a shadow-perturbed radiometric quantity, $\bar{\mathfrak{P}}$, evaluated at an in-water point P, and the corresponding shadow-free quantity, $\mathfrak{P}$, evaluated exactly as for $\bar{\mathfrak{P}}$, but in the absence of the AAOT structure. The PRE is indicated by $\varepsilon_{\mathfrak{P}}$, and is defined as

$$\varepsilon_{\mathfrak{P}} \;=\; 100\,\frac{\mathfrak{P}-\bar{\mathfrak{P}}}{\mathfrak{P}}, \qquad (4)$$

where, in general, $\bar{\mathfrak{P}}$ and $\varepsilon_{\mathfrak{P}}$ may show an explicit dependence on the (x, y, z) position coordinates of $\mathfrak{P}$. For the present system, the y-dependence was dropped, because the profiles are all performed along constant y. The z-dependence was also dropped, because the PRE values are evaluated at a given depth.

Shadow-free conditions can be easily modeled through MC simulations; in contrast, they are difficult to determine experimentally, because of practical limitations associated with deploying a free-fall system in shallow water at the end of a long cable. The *in situ* shadow-free location is ideally located an infinite distance from the tower. More realistically, it can be located at a finite *far-field* distance. The comparison between the far-field data and those perturbed by the tower at distance x can be made by assuming the water mass is homogeneous along its horizontal planes (i.e., the horizontal variation in IOPs is assumed negligible).

The radiometric quantities $\mathfrak{P}$ and $\bar{\mathfrak{P}}$ are in-water radiances and irradiances, normalized with respect to the incident above-water solar irradiance data, and are used for the comparison of *in situ* versus simulated PRE results (i.e., for the measurement–model comparison). The normalization is introduced to account for any atmospheric illumination change occurring during data collection.

3.3 *IN SITU* METHODS

The experimental evaluation of the tower shading perturbations relied on the use of miniNESS data deployed at sequential distances from the tower. The quantitative use of these data required three major elements:

1. Quality assurance of the data (which included preprocessing and subsequent quality control procedures),
2. Depth smoothing and binning of the radiometric quantities, and
3. Application of nonlinear fitting procedures for spatial interpolation.

The detailed aspects of these elements are presented in the following sections.

The optical data were collected as a series of experiments, which were composed of a sequence of casts (Table 2). In most cases, the distance from the tower was varied, but two experiments were executed at a constant distance from the tower, so the contribution of environmental variability could be assessed. The latter experiments were conducted at $x = 7.5$ m, which corresponds to the same distance where the WiSPER data are collected, so these data also allow for a good comparison with WiSPER data.

Table 2. A summary of the miniNESS experiments executed in the second tower-shading campaign showing the casts involved for each experiment, the time periods covered, and the range in distance away from the tower, x. Experiments 7 and 13 were executed at a constant distance of 7.5 m.

Exp.	*Casts*	*SDY*	*Time* [GMT]	x [m]
1	2– 6	191	0855–0902	3 → 9
2	7– 14	191	1128–1135	3 → 15
3	15– 30	191	1151–1220	3 → 29
4	31– 44	191	1222–1235	27 → 3
5	45– 56	191	1245–1256	3 → 23
6	57– 69	191	1258–1313	23 → 3
7	70– 80	191	1316–1329	7.5
8	81– 92	194	1037–1050	3 → 21
9	93–103	194	1104–1112	3 → 21
10	104–114	194	1113–1122	21 → 3
11	115–125	194	1123–1132	3 → 21
12	126–136	194	1133–1142	21 → 3
13	137–147	194	1144–1153	7.5
14	148–158	194	1216–1231	3 → 21
15	159–169	194	1246–1300	3 → 21
16	170–180	194	1301–1319	21 → 3
17	181–191	194	1417–1434	3 → 21
18	192–206	195	0807–0822	3 → 29
19	207–221	195	0824–0846	29 → 3
20	222–232	195	0946–0958	3 → 21

Note: Cast 1 was executed as a test of the instrument and the deployment system.

3.3.1 Optical Data Processing

The optical data processing is composed of four steps: a) preprocessing to create the calibrated values, b) depth smoothing and binning to remove noise, c) construction of fixed-depth profiles as a function of distance, and d) quality control procedures. Experimental error was determined using nonlinear curve fitting procedures and the identification of confidence bands. Cast sequences, representative of different measurement conditions, were selected for the shadowing analysis and are presented in Chapt. 4, along with summary results.

3.3.1.1 Preprocessing

Two types of optical data were collected. The so-called *dark* or *offset* values were recorded with caps on the radiometers (for 3 min), and *raw* or *signal* values were collected with caps off during optical profiling. The offset data are denoted by the O superscript and the raw data by the R superscript. For example, $E_d^O(0^+,\lambda)$, $E_d^O(0,\lambda)$, $L_u^O(0,\lambda)$, and $p^O(0,\lambda)$ are the offset values for the above-water solar irradiance, in-water downward irradiance, in-water upwelling radiance, and pressure, respectively. The offset values were averages used to establish the null or zero level of the sensors. In the case of the pressure sensor, the offset is the so-called *pressure tare*.

The calibration files provided by the manufacturer (Satlantic, Inc.) for the miniNESS optical sensors included the spectral scale factors, denoted by the superscript S, and immersion factors, denoted by the superscript I. The calibration file also included a scale factor for the pressure gauge (p^S) and coefficients for the tilt sensors.

The net digital counts were computed as the difference of the signal values minus the offset values. The (linear) calibration coefficients were used to convert the net digital counts into absolute (calibrated) geophysical units (Table 3), where the latter are identified by the C superscript. The depth values of the calibrated radiometric data were adjusted to account for the fixed distance offset between the miniNESS pressure gauge and the light sensors (i.e., E_d and L_u). The C superscript is hereafter dropped from symbols referring to calibrated optical data.

Table 3. The transformations applied to convert the raw (digital counts) data into absolute geophysical units. The calibrated vertical tilt of the miniNESS profiler, φ^C, is derived from the calibrated x and y two-axis tilts, φ_x^C and φ_y^C, respectively.

Symbol	*Formulation and Units*
E_d^C†	$E_d^S\,E_d^I\left(E_d^R - E_d^O\right)\ \left[\mu\mathrm{W\,cm^{-2}\,nm^{-1}}\right]$
L_u^C	$L_u^S\,L_u^I\left(L_u^R - L_u^O\right)\ \left[\mu\mathrm{W\,cm^{-2}\,nm^{-1}\,sr^{-1}}\right]$
p^C	$p^S\left(p^R - p^O\right)\ \left[\mathrm{m}\right]$
φ_x^C	$c_{x0} + c_{x1}\left(\varphi_x^R\right) + c_{x2}\left(\varphi_x^R\right)^2\ \left[^\circ\right]$
φ_y^C	$c_{y0} + c_{y1}\left(\varphi_y^R\right) + c_{y2}\left(\varphi_y^R\right)^2\ \left[^\circ\right]$
φ^C	$\tan^{-1}\left(\tan^2\varphi_x^C + \tan^2\varphi_y^C\right)^{1/2}\ \left[^\circ\right]$

† For the above-water solar irradiance sensor, $E_d^C(0^+)$, the immersion factor is, by definition, unity.

To remove perturbations induced by changes in the light field during the execution of multiple miniNESS profiles, the in-water optical measurements were normalized with respect to the solar irradiance according to:

$$E'_d(x,z,\lambda,t) \;=\; \frac{E_d(x,z,\lambda,t)}{E_d(0,0^+,\lambda,t)}E_d(0,0^+,\lambda,t_0), \qquad (5)$$

and

$$L'_u(x,z,\lambda,t) \;=\; \frac{L_u(x,z,\lambda,t)}{E_d(0,0^+,\lambda,t)}E_d(0,0^+,\lambda,t_0), \qquad (6)$$

where the factor $E_d(0,0^+,\lambda,t_0)$ is applied to preserve the physical units of the normalized quantities, and t_0 denotes the starting time for the first cast in the sequence of casts defining a single experiment.

3.3.1.2 Smoothing and Binning

The noise in the normalized optical profile data were primarily induced by wave-focusing effects and excessive instrument tilts. Assuming the noise is equally distributed between high and low values, it was reduced with a seven-point *moving-box* arithmetic averaging filter. Given the sampling frequency (6 Hz) and the descent speed of the profiler (about $0.6\,\mathrm{m\,s^{-1}}$), each *box* in the filter corresponds to a vertical extent of approximately 10 cm.

The depth coregistration of the profile data was accomplished through data binning. The $E'_d(x,z,\lambda,t)$ and $L'_u(x,z,\lambda,t)$ data were binned at discrete depths, z_i, using depth intervals of 0.5 m (ranging from $z_i - 0.25$ m to $z_i + 0.25$ m) resulting in $E'_d(x,z,\lambda,t_i)$ and $L'_u(x,z,\lambda,t_i)$ values, where t_i is the average time for each binning interval associated with depth z_i. In-water profiles of the hydrographic and IOP data were binned accordingly.

3.3.1.3 Fixed-Depth Profiles

The optical profiles within a single experiment were sequentially ordered as an increasing function of x. Optical data sequences at constant depth were then generated from each set of the in-water profiles for each experiment. A fixed-depth cross section is hereafter referred to as *distance-profile*.

A typical AAOT shadow-perturbed distance-profile, in this case taken from experiment 4 (SDY 191), is shown in Fig. 6a. The plot displays, for the nominal channel at 490 nm, the E'_d and the L'_u values as a function of x and at a fixed depth $z = 10$ m. During experiment 4 the water column was stratified and turbid, with little wave-focusing effects, and the sky was clear. The cast at $x = 23$ m was affected (at 10 m depth) by a tilt greater than 7°, so it was flagged and not considered.

A general feature can be seen in Fig. 6a, which is superimposed upon the underlying noise: there is a falloff in the radiometric signal as the sensor distance with respect to the tower decreases. Indeed, the AAOT structure exhibits a remarkable shadowing influence on the in-water radiometry: at 7.5 m distance (the deployment position for WiSPER) the irradiance drops to $0.060\,\mu\mathrm{W\,cm^{-2}\,nm^{-1}}$ (from 0.070 at 27 m), which represents a 14% decrease. Over the same interval, the radiance value drops from 0.00060 to $0.00045\,\mu\mathrm{W\,cm^{-2}\,nm^{-1}\,sr^{-1}}$, which is a 25% decrease.

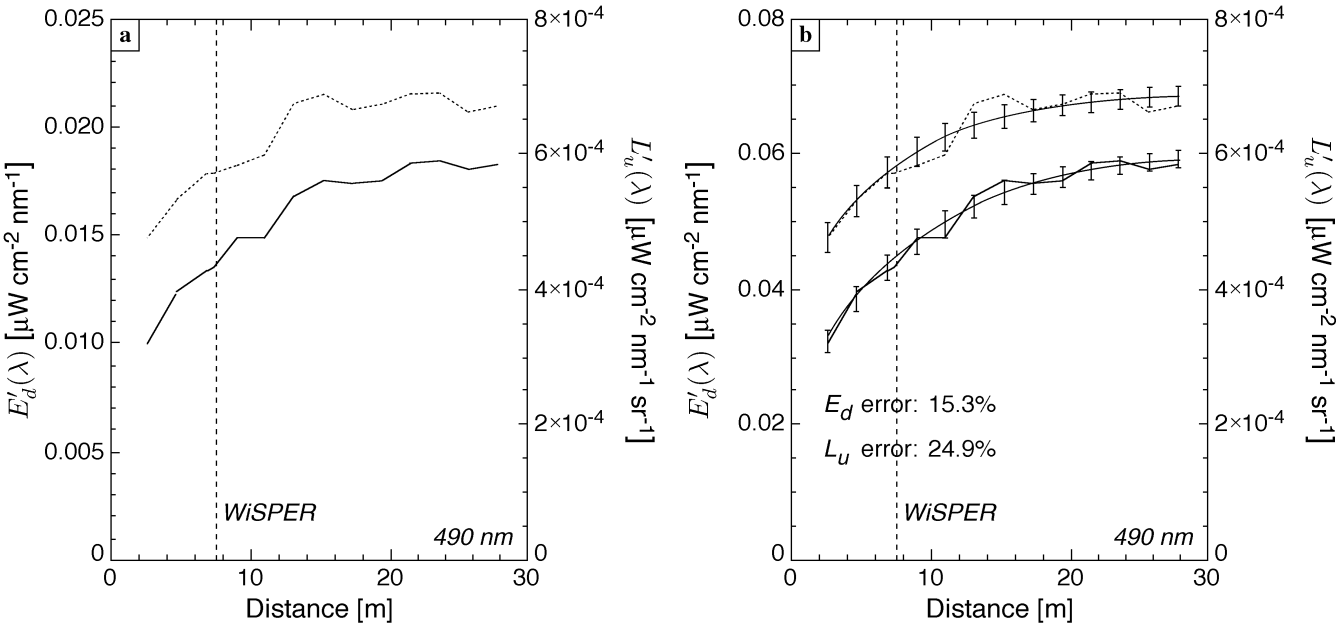

Fig. 6. Typical fixed-depth AAOT shadow-perturbed distance-profile plot for $\lambda = 490\,\text{nm}$ as a function of distance x from the tower, and at a fixed depth $z = 10\,\text{m}$: **a)** the radiometric quantities E'_d (dotted line and left scale) and L'_u (solid line and right scale), and **b)** the fitted curves and error bars added to the radiometric quantities. The dashed vertical line indicates the distance, 7.5 m from the AAOT structure, where WiSPER is routinely deployed.

It is important to note these shadowing estimates are computed using only two data points at 7.5 m, and at 27 m (i.e., the *far-field* value). This means that any noise affecting the considered data strongly influences the computed shadowing perturbation effects. Similar evaluations based on a different far-field distance (or on the same distance but for a repeated experiment) could, therefore, produce different shadowing effects at the same investigation point. An improved shadowing evaluation procedure is proposed later on using data fitting to minimize noise effects on (fixed-depth) distance-profile data.

3.3.1.4 Data Quality Control

Quality control of the *in situ* data is performed to ensure their proper selection for consistent comparison with modeled data. The analysis of E_d and L_u depth profiles showed that for several experiments of the first tower-shading campaign (Zibordi et al. 1999), the shadowing effects were masked by the presence of mucilage which was observed during many of the optical casts.

Mucilage occurs as highly scattering and inhomogeneous thick layers of gelatinous aggregates (Molin et al. 1992), which induce spatial and temporal variability within the in-water light field and is a recurring feature of the northern Adriatic Sea in the summer months (Berthon et al. 1999). The multiple profiles taken in the absence of mucilage, and at a variety of distances from the tower, showed almost regular and correlated variations, while the multiple profiles taken in the presence of mucilage showed irregular variations with respect to both distance and depth. Experiments presenting such distance and depth irregularities were not included in the data analysis.

An examination of some E'_d and L'_u profiles showed higher noise for the data within the topmost water layer, which was probably a consequence of more pronounced wave effects in this layer with respect to the others. Further analysis of optical profiles also revealed some were degraded by stratification and bottom effects, which induce a change as a function of depth in the normal decay of the optical signal. Consequently, any profiles subjected to these three sources of degradation were rejected for further analysis.

In addition, data close to the red portion of the spectrum, where the in-water signal, especially at depth, suffers more from low counts (i.e., high instrument noise) and from Raman scattering effects not accounted for within the MC simulations, were not retained. Another criteria applied in the quality assurance of *in situ* data, was the removal of data acquired with large tilts, i.e., $\varphi > 7°$.

3.3.2 Experimental Uncertainties

Experimental parameters that are important in obtaining absolute radiometric comparisons between field and modeled data (but were not available) are the in-water scattering phase function, the AAOT reflectivity, the effective skylight distribution, and the uncertainty in sensor

features, e.g., the non-ideal cosine response of the irradiance collectors. These factors, however, do not generally vary during an experiment, so they were assumed to not significantly influence the intercomparison between simulated and measured data through the proposed approach based on the far-field normalization.

The experimental distance-profile E'_d and L'_u data fall close to smooth monotonic curves. Such ideal curves would be obtained experimentally if all the sources of disturbance (e.g., wave focusing, horizontal inhomogeneities, excessive sensor tilts) were removed or at least minimized.

An error minimization procedure is, therefore, needed to remove the source of variability within single experiments. This procedure is illustrated in the following sections, where a multiparameter, nonlinear curve fitting algorithm is presented as applied to the distance-profile data. The method applied for the determination of a nonlinear confidence band is also described.

3.3.2.1 Curve Fitting Distance-Profile Data

The quantification of the *in situ* PRE at the distance from the tower at which the radiometric quantities can be assumed uncontaminated by the superstructure needs to be defined. The selection of one fixed reference distance, which is assumed unperturbed, is one way to quantify the experimental shadowing effects. This approach may not always be satisfactory, because unperturbed points are not always located at the same position for all experiments. It is, therefore, preferable to adopt a procedure, by which an *optimal* fitting curve may be drawn through all the experimental data, and then to evaluate PRE values from the fitted values. In this case, all the deployment distances provide equal weight to the final shadowing curve, and the evaluated PRE is less dependent on the noise affecting single data points.

To minimize surface wave and bottom perturbations, the analysis of E'_d and L'_u distance-profiles was generally carried out using depth bins at intermediate depths between the sea surface and the sea floor.

3.3.2.2 The Fitting Function

The choice of a fitting function was made based on its capability of reproducing the tower shading perturbations as a function of distance. A multiparameter, nonlinear (*mechanistic*) growth model, which links the independent variable x (position) with the dependent variable ω (light intensity), through the so-called *monomolecular* growth function, was chosen:

$$\omega \;=\; \alpha\left(1 \;-\; \beta\, e^{-\gamma x}\right), \tag{7}$$

where α, β, and γ are positive parameters.

The monomolecular growth function is also called the Box-Lucas growth function (Draper and Smith 1981) and arises from the integration of

$$\frac{d\omega}{dx} = \;\gamma\left(\alpha \;-\; \omega\right), \tag{8}$$

where, $d\omega/dx$ is the growth rate of the light intensity signal ω (radiance or irradiance) with respect to the position x. This function defines the growth rate to be directly proportional, through γ, to the amount of growth yet to be achieved, $\alpha - \omega$. This indicates that an asymptotic flattening of the curve occurs at large x values.

The parameter α represents the upper limiting value to the growth function, and for $x = 0$, the curve starts at the value $\alpha(1-\beta)$. In this model, the growth rate linearly decreases with increasing ω. Because of these features, the growth function is assumed to be adequate to describe the AAOT shading effects as a function of the distance from the superstructure.

3.3.2.3 Fitting Procedures

A pre-existing nonlinear, least-squares fitting routine (`non-lin-lsq.pro`), available as a part of the Interactive Data Language (IDL) software package from Research Systems, Inc. (Boulder, Colorado), was adopted to iteratively determine the fitting parameters in (7). This routine is based on a Marquardt-type algorithm (Marquardt 1963), which uses a fitting method based on the the gradient-expansion algorithm (which combines the best features of the gradient search with the method of linearizing the fitting function).

The iterative fitting procedure stops when the convergence of the *goodness of the fit* (χ^2) is to within 0.1%. The results of the iterative procedure are the average best-fit parameter values, the standard deviations of the fitting parameters, and the variance-covariance matrix of the fitting parameters.

The best-fit parameters are used to draw the interpolating curves (Fig. 6b). The remaining information is used, as described in Appendix B, to determine the error bars associated with the curves. Figure 6 also highlights that the *in situ* noise can be minimized with averaging. Successful noise reduction means a lower bias is introduced in the evaluation of the signal intensity as a function of distance, and the renormalization to a value at a fixed reference distance is not necessary. In fact, the shadow-free *in situ* distance can be assumed to occur where the steepness of the regression curve is less than a given threshold value.

Values of $\varepsilon_{\bar{\mathfrak{P}}}$ are given in Fig. 6b for E'_d and L'_u as "E_d error" and "L_u error," respectively, and evaluated at the fixed 7.5 m WiSPER profiling distance. These are the PRE values, given by

$$\begin{aligned}\varepsilon_{\bar{\mathfrak{P}}}(7.5) \;&\approx\; \varepsilon'_{\bar{\mathfrak{P}}}(7.5)\\ &=\; 100\,\frac{\mathfrak{P}'(X) \;-\; \bar{\mathfrak{P}}(7.5)}{\mathfrak{P}'(X)},\end{aligned} \tag{9}$$

and calculated by approximating the experimental shadow-free $\mathfrak{P}$ quantities with the quasi-unperturbed $\mathfrak{P}'$ quantities computed along the extrapolated fitting curve at a distance

$x = X$ at which the perturbed $\bar{\mathfrak{P}}$ value increases by less than 0.1% for a 1 m distance increase, i.e., where X is such that $\varepsilon_{\bar{\mathfrak{P}}}(X+1) - \varepsilon_{\bar{\mathfrak{P}}}(X) < 0.1\%$. The $\varepsilon_{\bar{\mathfrak{P}}}(7.5)$ *in situ* values are, therefore, dependent on X, and are obtained separately for each shadowing experiment, making use of the specific set of best-fit function parameters.

3.3.2.4 Fitting Difficulties

It is possible that high noise values at a specific distance x, may significantly influence the determination of the regression curve, thereby shifting the retrieved quasi-unperturbed point farther from, or closer to, the tower than the real shadow-free point would be. To minimize the effects of this added source of uncertainty, a solution is to relax the parameters of the interpolating curves while keeping their values consistent.

The problem of determining the predefined variability of the interpolating curve between two given points is not different from evaluating the error bars, to a given degree of confidence for all points along the fitted curve. These error bars are referred to as "confidence bands," because the curves may be drawn within them to a given degree of confidence, but still respecting the fit. Evaluating the confidence bands allows for a consistent comparison with MC simulated data, which present inherent statistical noise. A confidence band approach was, therefore, undertaken.

3.3.2.5 Nonlinear Fit Confidence Bands

Once the curve fitting algorithm has provided a converging set of parameters describing the interpolating curve, there remains the problem of assessing to what degree of confidence such a curve represents the actual shadowing effects and, thus, identifies an error bar for the *in situ* shadowing PRE. A confidence level of 95% was chosen, so that error bars were immediately comparable with the 2σ error bar on the MC statistical responses, where σ is the estimated standard deviation of the mean radiometric quantity from MC computations (Spanier and Gelbard 1969).

The basic elements describing the methods applied for the determination of confidence bands in the multiparameter fitting theory, are provided in Appendix C. Example error bars on a fitted curve are shown in Fig. 6b, where these error bars are defined at the 95% confidence level (i.e., $\vartheta = 0.05$). Shadowing PREs, given in the plot for E_d and L_u at $x = 7.5$ m, were calculated using the fitting curves.

3.4 SUMMARY

Tower-shading effects for the AAOT are described using the PRE between a shadow-perturbed radiometric quantity, $\bar{\mathfrak{P}}$, evaluated at an in-water point P, and the corresponding shadow-free quantity, $\mathfrak{P}$, evaluated exactly as for $\bar{\mathfrak{P}}$, but in the absence of the AAOT structure. The comparison of simulated and *in situ* radiometric data is accomplished using backward MC simulations of radiative transfer processes of the atmosphere–ocean–AAOT–detector system for the former and miniNESS profile data for the latter. The MC simulations account for: a) atmospheric and oceanic IOPs, b) vertical stratification, c) detailed AAOT geometry (although spectral reflectivity of the structure was assumed zero), and d) the actual instrument geometry and sensor field of view together with its light-collecting properties.

The experimental determination of tower-shading perturbations through miniNESS data relies on deployments at sequential distances from the tower. The quantitative use of these data required: a) a quality assurance of the observations, b) depth smoothing and binning, and c) the application of nonlinear fitting procedures for spatial interpolation. The optical profiles belonging to the same experiment, defined as a sequence of profiles at increasing distance from the platform, were sequentially aligned as a function of the distance from the main tower structure. Optical data sequences at constant depth were generated from each set of in-water profiles for each experiment.

The fixed-depth cross sections, referred to as *distance-profiles*, showed the radiance and irradiance data closely followed smooth monotonic curves which increased with increasing distance from the tower. The curves included random, overlapping noise from the perturbing effects of wave focusing, horizontal inhomogeneities, and excessive sensor tilts. To minimize uncertainties induced by these perturbations, an error minimization procedure, based on a multiparameter, nonlinear curve-fitting algorithm, was developed for the distance-profile data.

Chapter 4

Preliminary Results

John P. Doyle†
JRC/Space Applications Institute
Ispra, Italy

Stanford B. Hooker
NASA/Goddard Space Flight Center
Greenbelt, Maryland

Giuseppe Zibordi
JRC/Institute for Environment and Sustainability
Ispra, Italy

Abstract

The measurements from three field experiments, collected under very different environmental conditions, compare well with simulated model data. Under extreme conditions, however, high uncertainties in the estimated results are produced by excessive instrument tilt and by wave-focusing effects. Shadowing perturbations for very clear waters are restricted to within 15–20 m from the tower legs for upwelling radiance and downward irradiance. The far-field unperturbed distance is reached at 20–25 m in relatively turbid waters. Under overcast conditions, the magnitude of the shadowing effect is larger than under clear sky conditions and the far-field distance is reached at approximately 30 m from the tower legs.

4.1 INTRODUCTION

A selection of data taken from the experiments conducted during the second AAOT tower-shading campaign in July 1998 (Table 2) are used for preliminary intercomparisons between field measurements and model results. The *in situ* conditions were chosen to represent, as comprehensively as possible, the environmental variability found at the AAOT site and to investigate the extent of the influence these diverse conditions have on the AAOT shadowing of radiometric data.

The data chosen for the case studies were taken from three distinct experiments, each one performed on a different day, and selected as follows:

1. Experiment 6 (SDY 191), stratified and highly attenuating waters, clear sky, and data parsed at 9 m depth for all casts;
2. Experiment 16 (SDY 194), homogeneous and very clear waters, clear sky (with haze), and data parsed at 8 m depth for all casts; and
3. Experiment 18 (SDY 195), homogeneous and attenuating waters, diffuse (overcast) sky, and data parsed at 2 m depth for all casts.

The data collected during these experiments and then parsed at the specified fixed depths are of a quality suitable for intercomparison with simulations, and cover a broad range of environmental parameters, i.e., in-water IOPs, solar zenith and azimuth angles, atmospheric optical depths, and illumination conditions. Quality control on selected distance-profiles were carried out to discard data affected by excessive tilts or wave-focusing effects.

Profiles of the *in situ* hydrographic (temperature and salinity) and IOP (spectral absorption and attenuation coefficients derived from AC-9 data) variables are provided in Figs. 7, 8, and 9 for experiments 6, 16, and 18, respectively. Associated with these plots, full profiles of *in situ* optical quantities perturbed by the tower shading are provided in Figs. 10, 11, and 12 for the same three experiments, respectively.

The culmination of the analysis for experiments 6, 16, and 18 are the fixed-depth plots of distance-profile radiometric data, which are provided in Figs. 13, 14, and 15, respectively. All of these figures show considerable shadowing effects: as x increases, i.e., as the distance from the tower increases, the fitted radiometric values increase

† Currently with Imperial College of Science, Technology and Medicine, Computational Physics and Geophysics, London, England.

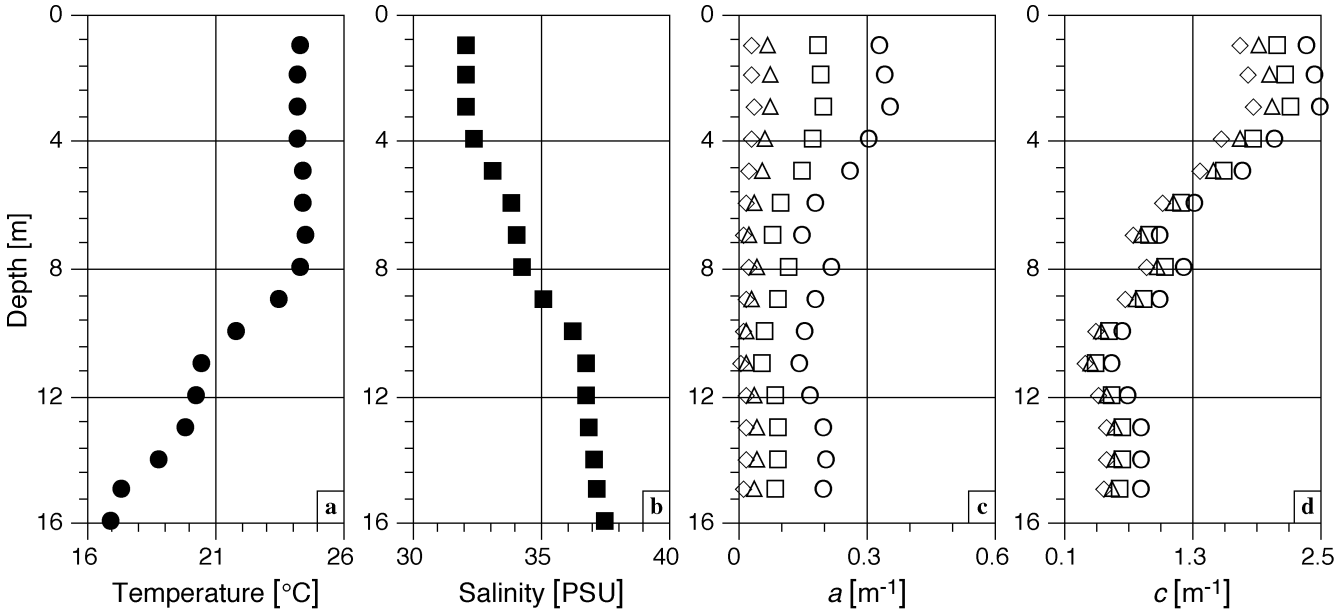

Fig. 7. Water column hydrographic and spectral IOP data for experiment 6 on SDY 191 (stratified and highly attenuating waters, plus a clear sky): **a)** temperature, **b)** salinity, **c)** absorption, and **d)** attenuation. For the latter two parameters, the symbols correspond to the nominal wavelengths of the measurements: 412 nm (circles), 490 nm (squares), 555 nm (triangles), and 650 nm (diamonds).

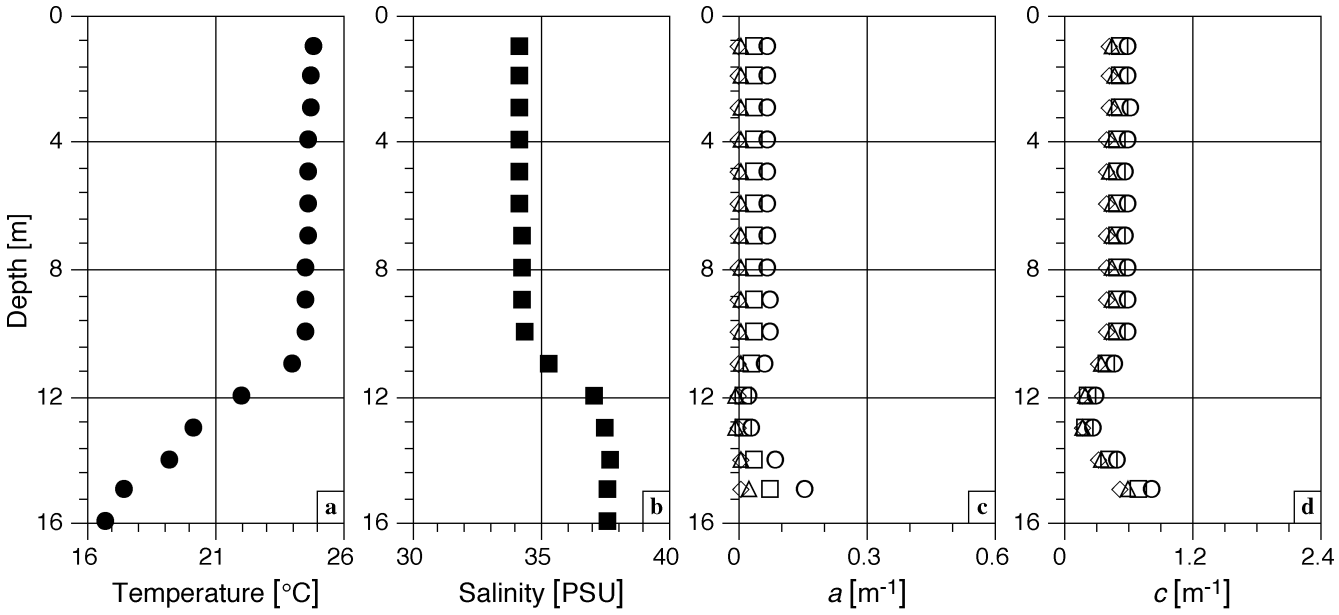

Fig. 8. Same as Fig. 7, but for experiment 16 on SDY 194 (homogeneous and very clear waters, plus a clear sky with haze).

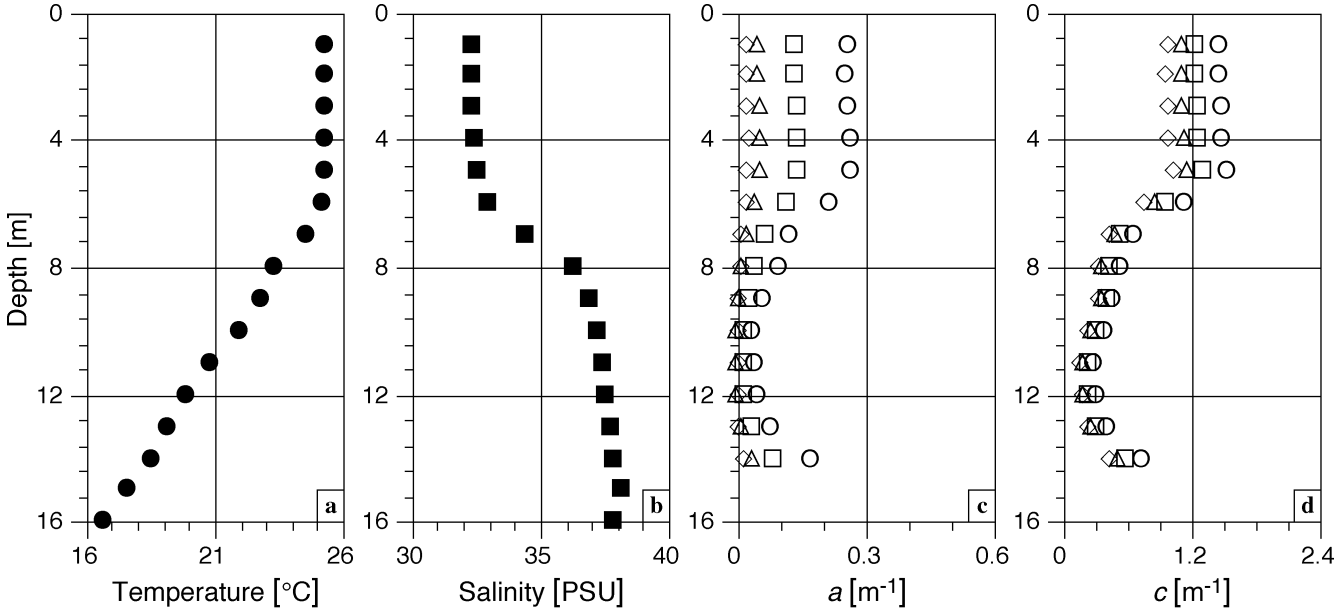

Fig. 9. Same as Fig. 7, but for experiment 18 on SDY 195 (very homogeneous and attenuating waters, plus a diffuse sky).

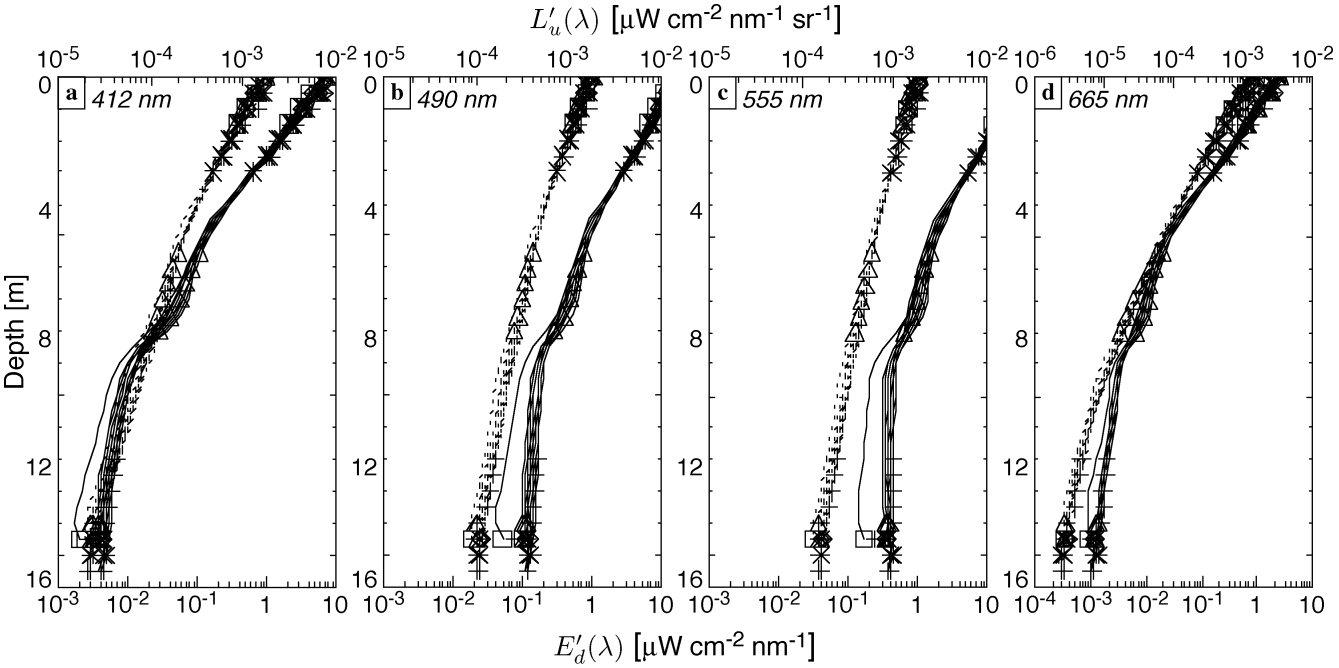

Fig. 10. Water column radiometric profiles for E'_d (dashed lines and bottom scale) and L'_u (solid lines and top scale) data for experiment 6 on SDY 191 (stratified and highly attenuating waters, plus a clear sky): **a)** 412 nm, **b)** 490 nm, **c)** 510 nm, and **d)** 665 nm. The symbols flag observations during high ($\geq 7°$) vertical tilts of the profiler.

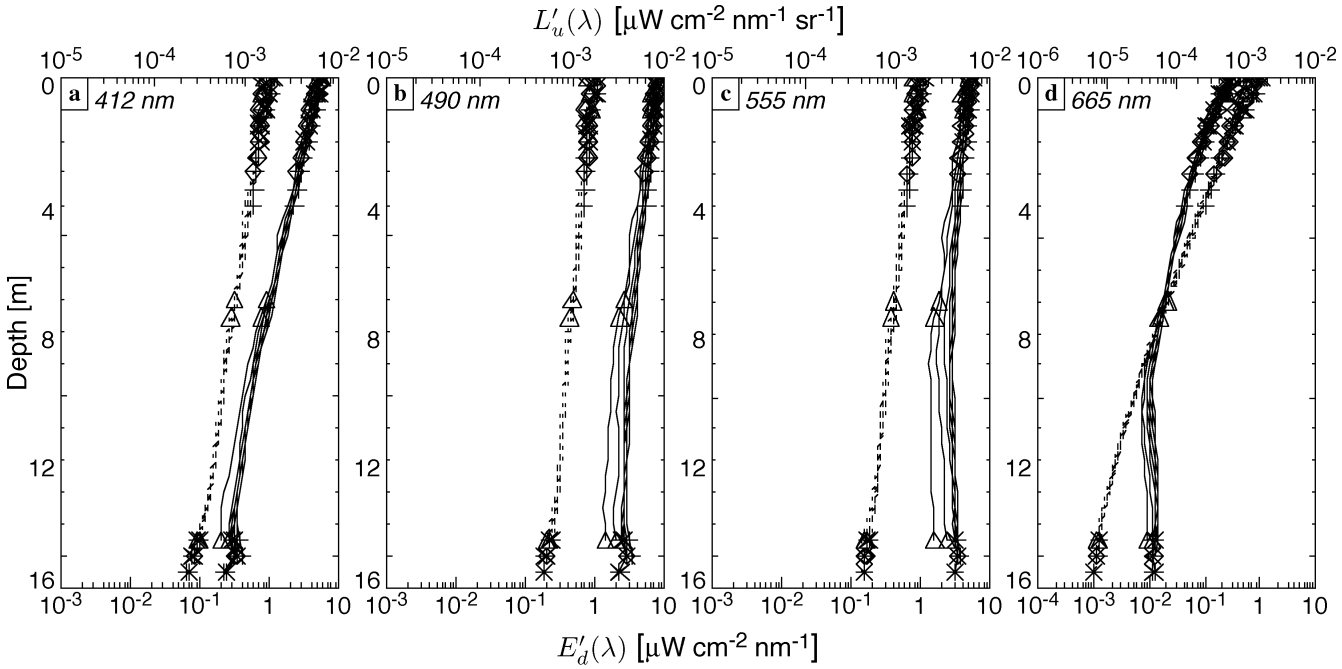

Fig. 11. Same as Fig. 10, but for experiment 16 on SDY 194 (homogeneous and very clear waters, plus a clear sky with haze).

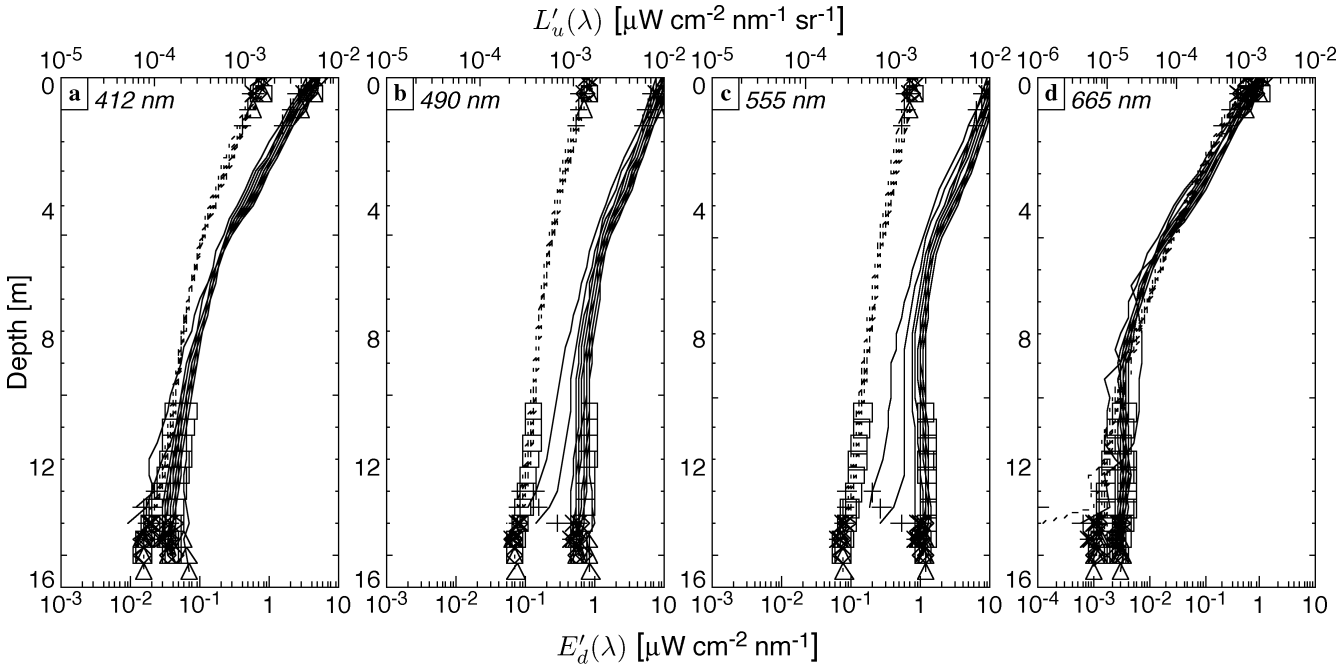

Fig. 12. Same as Fig. 10, but for experiment 18 on SDY 195 (very homogeneous and attenuating waters, plus a diffuse sky).

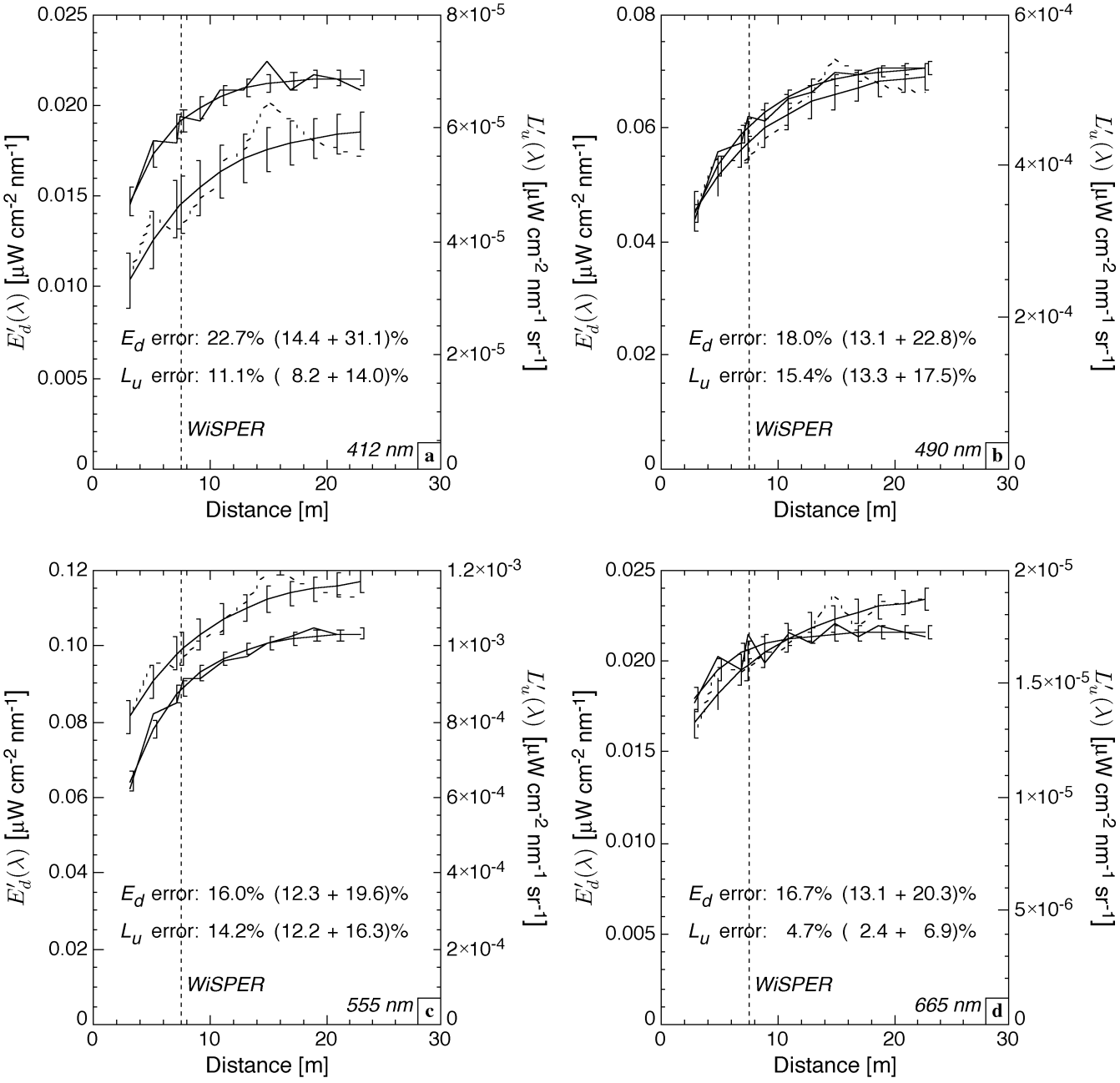

Fig. 13. Spectral E'_d (dashed line and left scale) and L'_u (solid line and right scale) distance-profiles (each one similar to the plot given in Fig. 6) for experiment 6 on SDY 191 (stratified and highly attenuating waters, plus a clear sky) at a fixed depth of 9 m and as a function of the distance from the tower: **a)** 412 nm, **b)** 490 nm, **c)** 510 nm, and **d)** 665 nm. Fitted curves and 95% confidence bars with shadowing PRE (and ranges) evaluated at 7.5 m. The vertical dashed line indicates the distance the WiSPER measurements are made.

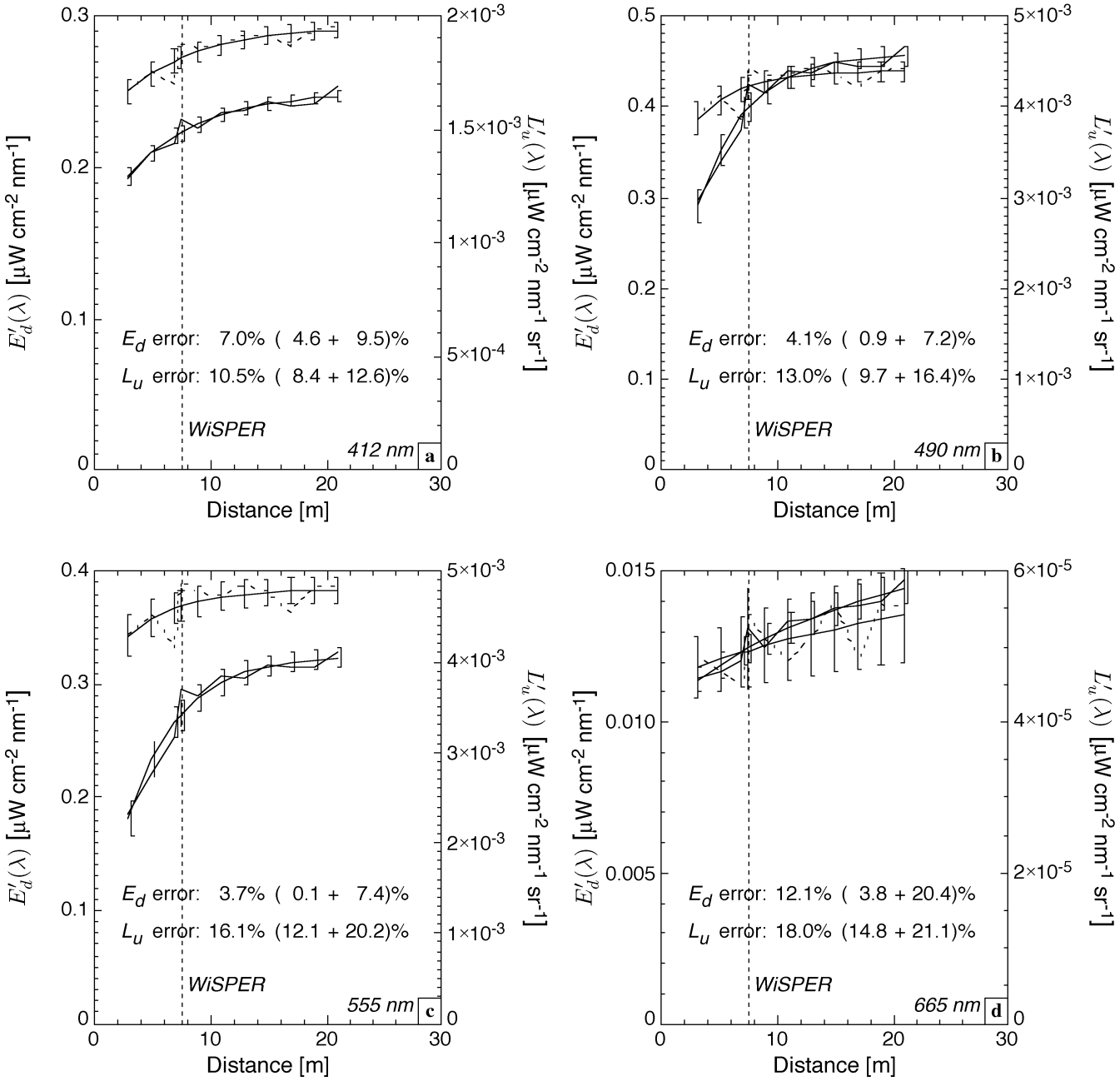

Fig. 14. Same as Fig. 13, but for experiment 16 on SDY 194 (homogeneous and very clear waters, plus a clear sky with haze), and a fixed depth of 8 m.

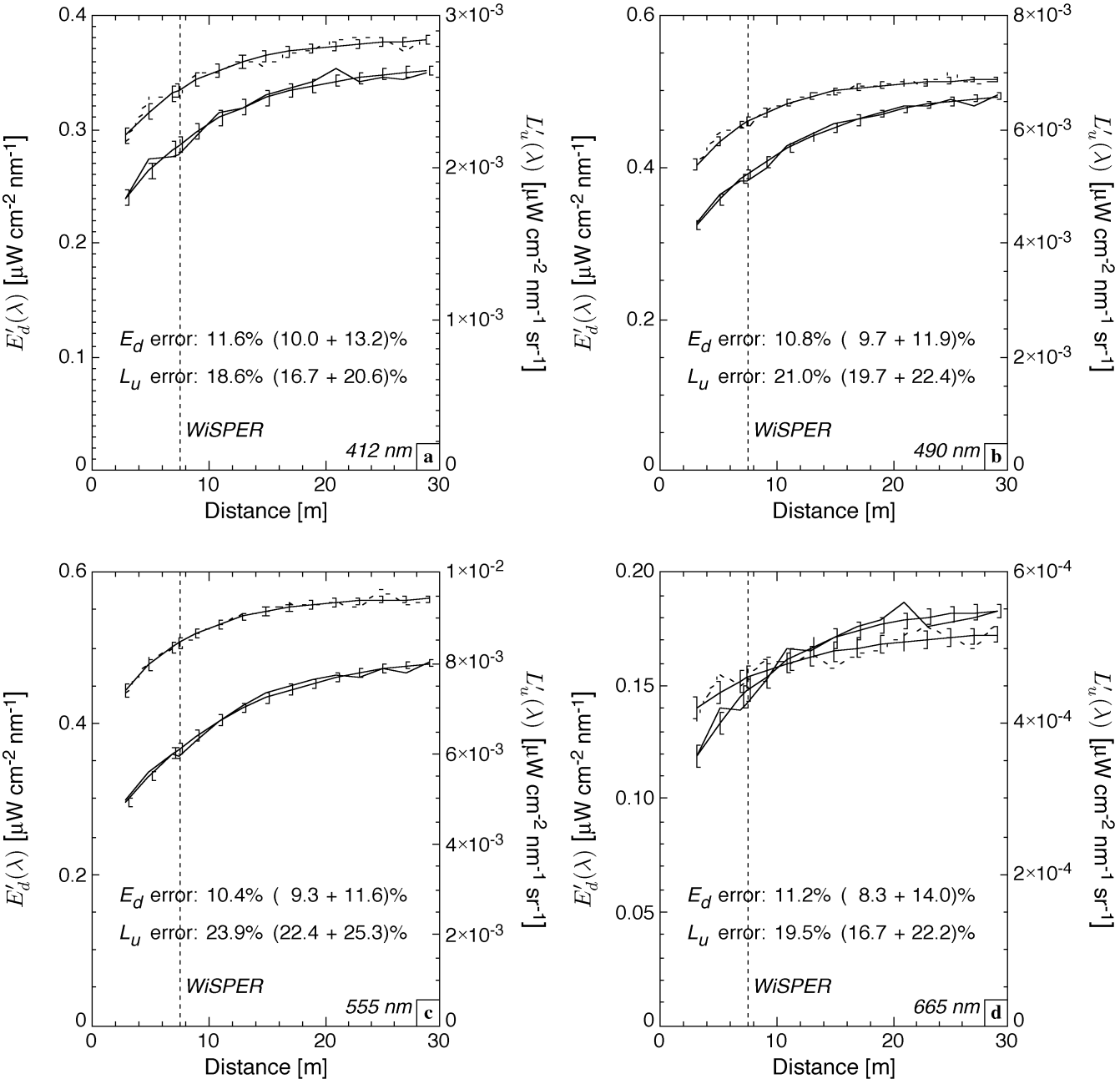

Fig. 15. Same as Fig. 13, but for experiment 18 on SDY 195 (very homogeneous and attenuating waters, plus a diffuse sky), and a fixed depth of 2 m.

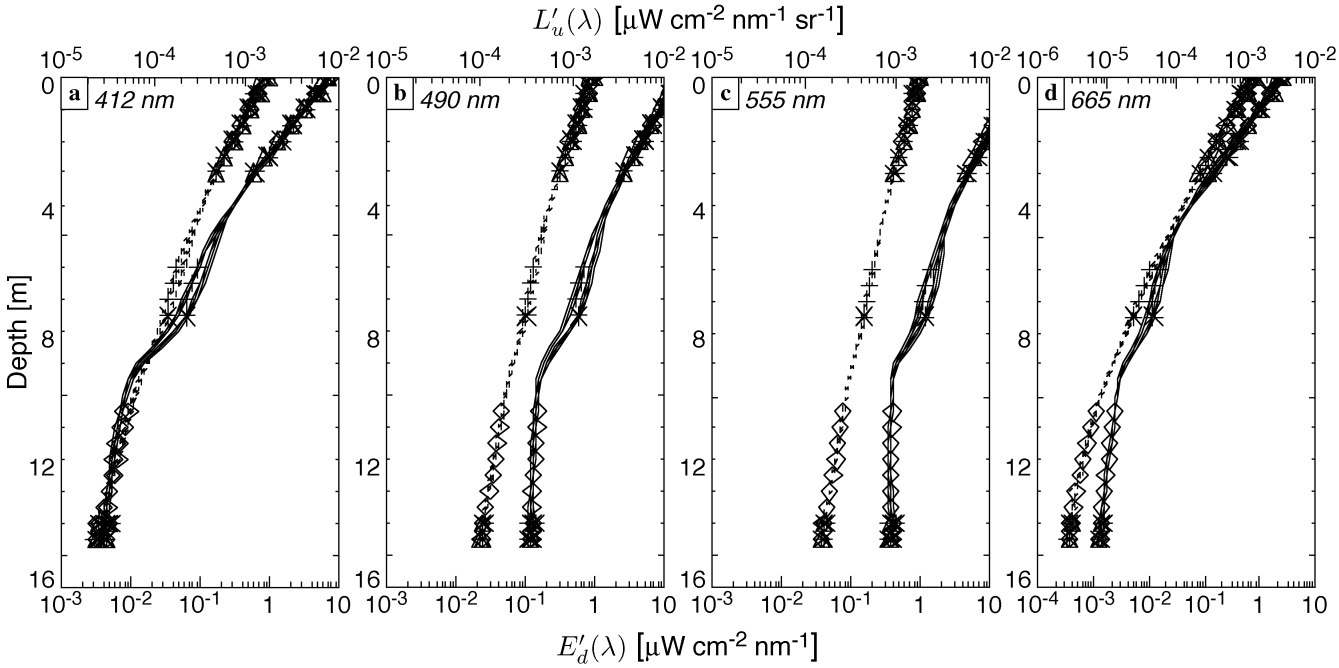

Fig. 16. Same as Fig. 10, but for experiment 7 on SDY 191 (characterized by stratified and highly attenuating waters and clear-sky conditions). This special experiment was performed by repeating 11 different casts, all at a 7.5 m distance from the tower. The water layer between 5–9 m depth was subject to rapidly varying IOPs, and the effect of this can be seen in the large variations of the radiance data from cast to cast within the layer. Distance-profiles falling within such unstable depth intervals should be rejected.

monotonically until they start to level off once the *far-field* distances are reached.

An additional experiment is presented to show the importance of water column stability and its influence on the reproducibility of the miniNESS measurements. Figure 16 displays the optical profiles for this additional experiment, during which all casts were sequentially repeated at the same distance (7.5 m) from the tower legs (experiment 7 on SDY 194). The figure shows that the data within the 5–9 m depth interval have a bimodal expression, in the sense that they follow one of two paths, whereas the data at other depths do not.

The distinctive variability in the 5–9 m depth interval is not due to varying illumination conditions. Normalization is applied to each cast and, moreover, such variations are unlikely to occur in exact coincidence with the time intervals involved during the 5–9 m depth sampling. Varying shadowing effects are also not a suitable explanation, because the casts are all repeated at the same location and in a relatively short time period.

The most likely reason for the variations observed in Fig. 16 is assumed to be a change in water properties (produced by water shears with distinctly different IOPs), introducing both time and space inhomogeneities. Consequently, the data in the 5–9 m depth layer were discarded in all experiments performed on SDY 194 and close in time to experiment 7. Although this is a recurring difficulty with trying to execute controlled experiments in the coastal environment, the advantages of having a stable platform (the tower) in an oceanic environment far outweigh any negative consequences associated with coastal variability.

4.2 AAOT SITE CONDITIONS

The AAOT site is located in a frontal region that can be characterized by either Case-1 or Case-2† water types (Berthon et al. 2002). The hydrological features of the area are primarily influenced by the northern river discharges, as well as by wind and rain variability. The horizontal homogeneity in the vicinity of the tower displays extremely different situations. There are time periods characterized by high spatial inhomogeneity and other time periods characterized by high spatial uniformity. Consequently, the *in situ* daily conditions are susceptible to very short timescale variations, which are superimposed on the main seasonal evolution.

Table 4 presents a summary of some environmental quantities measured at the AAOT site during the second tower-shading campaign. Although some of the variables

† The optical properties of Case-1 waters are solely determined by the phytoplankton and its derivative products (Morel and Prieur 1977), whereas Case-2 optical properties are also determined by other material, e.g., from terrestrial or bottom origin.

are not immediately important to the analyses presented here, they are presented for completeness and to show the extent of certain quantities. For example, the solar zenith angle, θ, spanned a wide range of 11.5–47.8°, but the wind speed, W, was usually low (less than $5\,\mathrm{m\,s^{-1}}$). Note the total chlorophyll a concentration, C_a, and the concentration of total suspended matter, C_{TSM}, show the water properties sampled included clear and turbid conditions, the optical consequences of which are well quantified by the diffuse attenuation coefficient, K_d. The sums of the particulate and yellow substance portions of the absorption and beam attenuation coefficients, $a_p + a_y$ and $c_p + c_y$, respectively.

Table 4. A summary of some environmental quantities measured at the AAOT site during the second tower-shading campaign. The K_d, $a_p + a_y$, and $c_p + c_y$ values are overall averages for 490 nm and for the day, where the ± values indicate the standard deviation in percent. The sea state is coded according to World Meteorological Organization (1983).

Parameter	*SDY 191*	*SDY 194*	*SDY 195*
Water Type	Case-2	Case-1	Case-2
C_a [$\mathrm{mg\,m^{-3}}$]	1.6	0.3	0.7
C_{TSM} [$\mathrm{g\,m^{-3}}$]	2.8	0.8	1.9
K_d [$\mathrm{m^{-1}}$]	0.32	0.08	0.23
	± 9.4%	± 12.5%	± 4.3%
$a_p + a_y$ [$\mathrm{m^{-1}}$]	0.16	0.03	0.10
	± 7.7%	± 3.8%	± 2.0%
$c_p + c_y$ [$\mathrm{m^{-1}}$]	2.14	0.55	1.26
	± 6.7%	± 3.1%	± 0.9%
Cloud Cover	0/8	0/8†	8/8
Illumination	Stable	Stable	Stable‡
θ [°]	11.5–34.2	23.2–47.8	28.5–42.2
Stratification	Strong	None	Strong
W [$\mathrm{m\,s^{-1}}$]	4.8	7.3	2.7
Sea State	1	1–2	1

† With haze. ‡ Slightly changing.

4.2.1 Experiment 6

Complex water stratification is observed quite clearly in Fig. 7 for SDY 191, and five main discrete layers can be roughly identified: 0–4 m, 4–6 m, 6–8 m, 8–11 m, and 11–15 m. The first (top) layer is probably sediment loaded, due to low salinity surface waters originating from terrigenous river out flow. Absorption and attenuation are both relatively high, which means water turbidity is generally high.

In this experiment, the solar zenith angle reached almost 30°, the solar azimuth angle, ϕ, was 235° and the sky conditions were clear. The Ångström coefficient and exponent were 0.07 and 1.5, respectively, giving an aerosol optical depth, $\tau_A(\lambda)$, of 0.26 and 0.19, at 412 and 510 nm, respectively. The atmospheric pressure was 1,016.0 hPa giving a (Rayleigh) molecular optical depth, $\tau_R(\lambda)$, of 0.32 and 0.16, at 412 and 510 nm, respectively. The ozone load was 327 Dobson units giving an ozone optical depth, $\tau_O(\lambda)$, of 6.6×10^{-4} and 1.4×10^{-4}, at 412 and 510 nm respectively. The former optical depth values were obtained by applying the models and relationships referenced in Doyle and Zibordi (2002).

Instrument tilts for experiment 6 are the worst for the three case studies, because of the presence of strong and varying underwater currents. The currents are also the cause for in-water IOP time variability, which is another source of *in situ* perturbations and inhomogeneity, as independently documented in experiment 7 (Fig. 16). Because of the time difference between IOP profiles carried out with the AC-9 instrument at the fixed profiling location, and the multiple casts performed with miniNESS, a discrepancy between assumed and actual IOPs is to be expected. This may become the source of measurement–model discrepancies.

In the 9 m fixed-depth profile (Fig. 13) a relatively low combined tilt (about 4°) occurs at a distance of 15 m, while a strong peak is present in the data at all wavelengths. This is probably associated with wave-focusing effects. This degrades the quality of the fitted curve, as shown by the large error bars in Fig. 13 (which are more pronounced for E_d than for L_u).

In summary, clear sky conditions combined with a relatively high turbidity of the water produced radiometric values smoothly increasing with distance from the AAOT structure, and thus producing pronounced shadowing effects.

4.2.2 Experiment 16

A moderate, and mainly stepwise, water stratification is observed in Fig. 8 for SDY 194. Three layers can be identified at 0–10, 10–13.5, and 13.5–15 m. The relatively thick homogeneous surface layer was produced by a storm occurring in the day preceding the experiment. Absorption and attenuation are both quite low, when compared to the average AAOT site values (Berthon et al. 2002).

In this experiment, θ reached about 30°, and $\phi \approx 235°$. Sky conditions were clear and relatively transparent: the Ångström coefficient and exponent values were 0.08 and 1.8, respectively, giving $\tau_A(\lambda)$ values of 0.39 and 0.27, at 412 and 510 nm, respectively. The latter values are about 50% higher than for SDY 191. Atmospheric pressure was 1016.2 hPa giving a $\tau_R(\lambda)$ of 0.32 and 0.16, at 412 and 510 nm, respectively; and the ozone load was 328 Dobson units giving $\tau_O(\lambda)$ values of 6.6×10^{-4} and 1.4×10^{-4}, at 412 and 510 nm, respectively (the same values as for SDY 191).

Instrument tilts rarely exceeded 5°, because the water currents around the tower were moderate. At intermediate distances, some spikes were observed with some data, and these are explained by surface gravity wave perturbations (the sea state was higher for experiment 16). The waves

have an impact on the quality of the fitted curve as can be seen by the relatively large error bars in Fig. 14, again more pronounced for E_d than for L_u.

In summary, clear sky conditions combined with a high water transparency (which were responsible for large wave-focusing perturbations), produced shadowing curves that saturated quickly, i.e., low shadowing effects.

4.2.3 Experiment 18

A stepwise IOP stratification is observed in Fig. 9 for SDY 195. Three water layers can be identified at 0–5 m, 5–11 m, and 11–15 m, with constant values for IOPs in the top layer, and smoothly decreasing and then increasing values in the two bottom layers. The river runoff caused by inland heavy rain was responsible for the sediment loaded top layer of freshwater characterizing data in Fig. 9. The previously well-mixed top layer present on SDY 194 has disappeared and, absorption and attenuation are now both relatively high in the top layer.

Sky conditions were completely overcast, presumably providing an almost totally uniform (i.e., isotropic) incident radiance distribution. The atmospheric pressure was 1004.7 hPa and the ozone load was 306 Dobson units. The fixed-depth profiles in Fig. 15 are at a depth of 2 m and suffer from significant tilts, but they did not produce any degrading effects because of the uniform sky light.

The overcast skies and relatively turbid waters produced radiometric data very smoothly increasing with distance from the AAOT structure. The shadowing curves, which saturate very slowly, produce very strong shadowing effects on the radiometric data.

4.3 DATA COMPARISONS

The MC simulations were performed within specific sun–atmosphere–ocean–tower–radiometer systems describing the particular environmental conditions present in the field during each of the tower shading experiments. *In situ* shadowing PREs are provided along with the 95% confidence intervals determined on the nonlinear function fitting the data, while MC simulated PREs are calculated with the $\pm 2\sigma$ statistical error interval (which accounts for the 95% probability that the average response falls within its bounds).

To provide preliminary measurement–model comparisons, the shadowing PRE values obtained from the simulation of radiometric quantities were compared to the corresponding *in situ* PRE values for experiments 6, 16, and 18. Despite the effort in producing accurate in-water profiles, a small number of casts appeared as outliers, that is, the derived optical parameters did not follow the expected monotonic growth of the shadowed signal as a function of increasing x. Outlying data from experiment 6 at a depth of 9 m, were easily identified and were not accounted for in the data analysis.

The E_d and L_u PRE values are presented spectrally for each radiometric quantity by giving the fitted or estimated value (ave.), along with the lowest (min.) and highest (max.) values computed according to the experimental confidence band interval or the simulated statistical spread interval. The measurement-model comparisons for experiment 6 are presented in Table 5 and show very good agreement at almost all wavelengths. In those cases where the agreement is degraded, it is associated with the (min. and max.) endpoints and not the central (ave.) value.

Table 5. Measurement and model comparisons for shading experiment 6 at 9 m depth. A representative set of wavelengths are shown rather than the complete set of seven measured by miniNESS.

λ and Results Type	$\varepsilon_{\tilde{E}_d}(\lambda)$ [%]			$\varepsilon_{\tilde{L}_u}(\lambda)$ [%]		
	Min.	*Ave.*	*Max.*	*Min.*	*Ave.*	*Max.*
412 Data	8.7	10.1	11.6	8.4	12.5	14.2
Model	*9.6*	*10.0*	*10.4*	*12.2*	*12.7*	*13.1*
490 Data	8.1	9.7	11.4	12.6	13.8	15.3
Model	*8.2*	*9.7*	*10.7*	*12.1*	*13.9*	*15.6*
555 Data	5.9	7.2	8.7	11.8	12.9	15.0
Model	*6.8*	*7.4*	*7.9*	*12.0*	*13.1*	*14.2*
665 Data	3.9	4.5	5.1	3.1	4.0	5.4
Model	*4.2*	*4.5*	*4.7*	*4.0*	*4.1*	*4.3*

Data from experiment 16 are optimal, because they are from near-ideal environmental conditions (transparent waters and clear sky conditions) and usually minimal profiler tilts. A relatively high tilt, however, affected the measurements in the first cast (at 3.5 m). When this *bad* measurement is removed from the fit, the experimental and simulation data are in excellent agreement, as shown in Table 6.

Table 6. Measurement and model comparisons for shading experiment 16 at 8 m depth, after removing an outlying data point from the experimental data processing.

λ and Results Type	$\varepsilon_{\tilde{E}_d}(\lambda)$ [%]			$\varepsilon_{\tilde{L}_u}(\lambda)$ [%]		
	Min.	*Ave.*	*Max.*	*Min.*	*Ave.*	*Max.*
412 Data	5.7	7.2	8.7	8.2	9.9	11.6
Model	*7.1*	*7.4*	*7.7*	*9.2*	*9.7*	*10.1*
490 Data	3.8	5.2	6.6	7.0	8.5	10.0
Model	*5.2*	*5.6*	*6.1*	*7.2*	*8.3*	*9.4*
555 Data	2.8	4.0	5.2	5.6	6.9	8.2
Model	*4.2*	*4.5*	*4.8*	*6.0*	*6.7*	*7.2*
665 Data	1.3	2.1	2.9	1.9	2.6	3.3
Model	*2.3*	*2.4*	*2.6*	*2.1*	*2.5*	*2.9*

Simulated data from experiment 18, the overcast situation, suffers from the assumption of an isotropic sky ra-

diance distribution. Departures from the assumed isotropicity are probably responsible for the simulations significantly overestimating the E_d shadowing PRE.

Table 7. Measurement and model comparisons for shading experiment 18 at a depth of 2 m.

λ and Results Type	$\varepsilon_{\tilde{E}_d}(\lambda)$ [%]			$\varepsilon_{\tilde{L}_u}(\lambda)$ [%]		
	Min.	*Ave.*	*Max.*	*Min.*	*Ave.*	*Max.*
412 Data	10.0	11.6	13.2	16.7	18.6	20.6
Model		*18.3*			*17.9*	
490 Data	9.7	10.8	11.9	19.7	21.0	22.4
Model		*17.7*			*16.8*	
555 Data	9.3	10.4	11.6	22.4	23.9	25.3
Model		*17.4*			*18.0*	
665 Data	8.3	11.2	14.0	16.7	19.5	22.2
Model		*17.2*			*16.2*	

4.4 CONCLUSIONS

The *in situ* data generally compared very well with the simulated values, although under extreme conditions allowance must be given for *in situ* uncertainties, mostly due to instrument tilts and wave-focusing effects. Attention also must be given to the possible presence of a significant nonisotropic atmospheric radiance distribution within an otherwise apparently ideal overcast sky. Keeping in mind such deviations from the modeled conditions, the majority of results from the *in situ* validation performed in this study are generally satisfactory, and support the use of the developed MC code to confidently assess shadowing corrections for a broad range of environmental and illumination conditions typically found at the AAOT site (Berthon et al. 2002).

Experimental evidence, acquired at a depth within the water column, indicates shadowing profiles for very clear waters (experiment 16) seem to flatten out for both L_u and E_d after 15–20 m from the tower legs. This *far-field plateau* is reached at 20–25 m in more turbid waters (experiment 6). Finally, under overcast conditions (experiment 18), the magnitude of the shadowing effect is significantly larger than under other conditions, and the far-field is reached at a distance of about 30 m from the AAOT legs. Following this study, it is advisable to deploy free-falling profilers in the solar direction at distances in excess of 30 m from the AAOT legs. Simulations confirm these findings.

At closer distances, for example at the 7.5 m deployment distance used for WiSPER measurements, the shadowing effect is notable even under clear-sky and clear-water conditions: both field and simulated data at a depth of 8 m and a wavelength of 490 nm show that with a solar zenith angle of 30°, the shadowing effect is within 4% for downward irradiance and within 13% for upwelling radiance.

Real-time Monte Carlo simulations, or look-up tables built from precomputed simulations, can be applied to the atmosphere–ocean–tower system to correct for shadowing perturbations in optical data collected in the proximity of the AAOT superstructure. Based on the validations presented in this study, the subsurface (0^- m) simplified system simulations, which are those carried out within the shadowing correction scheme proposed by Doyle and Zibordi (2002), are expected to accurately reproduce the measurements at the corresponding depth (i.e., those extrapolated to the 0^- m level). A good accuracy is also expected when measurements are conducted under sampling conditions differing from those considered in this study.

Acknowledgments

The participation of JRC and CNR personnel in the tower-shading field campaigns was primarily supported by the European Commission through contracts ENV4–CT96–0307 and MAS3–CT97–0087.

Appendices

A. In-Water Tower Perturbation Science Team
B. Multiparameter Confidence Bands
C. Nonlinear Confidence Bands

Appendix A

In-Water Tower Perturbation Science Team

The in-water tower perturbation science team members are presented alphabetically.

John Doyle
ICSTM/Earth Science and Engineering
Exihibition Road
London, SW7 2AZ
UNITED KINGDOM
Voice: 44–207–594–6387
Net: `j.doyle@ic.ac.uk`

Stanford Hooker
NASA/GSFC/Code 970.2
Bldg. 28, Room W126
Greenbelt, Maryland 20771
Voice: 301–286–9503
Fax: 301–286–0268
Net: `stan@ardbeg.gsfc.nasa.gov`

Dirk van der Linde
JRC/IES/IMW T.P. 272
I–21020 Ispra (VA) ITALY
Voice: 39–0–332–785–362
Fax: 39–0–332–789–034
Net: `dirk.vanderlinde@jrc.it`

Giuseppe Zibordi
JRC/IES/IMW T.P. 272
I–21020 Ispra (VA)
ITALY
Voice: +39–0–332–785–902
Fax: +39–0–332–789–034
Net: `giuseppe.zibordi@jrc.it`

Appendix B

Multiparameter Confidence Bands

A concise summary of the basic quantities and formulations, in multiparameter fitting theory, required to build the confidence bands for the fitted curve, follows the presentation of Draper and Smith (1981). Only essential reasoning and operative results are given here.

Let m be the number of experimental *in situ* observations (here about 15 data pairs), and n the number of parameters to be considered in the fit (here 3). The number of degrees of freedom of the fitting procedure is, thus, $m - n$. Let u be the vector of m independent variables (the distance from the tower), v the vector of m corresponding dependent variables (the shadowed irradiance, for instance), q be the vector of n parameters, and $f(u;q)$, a vector function of the vector variable u and parameter q, i.e., the nonlinear function adopted for the fitting procedure. For this study, the latter is the nonlinear monomolecular growth function ω in (4).

The m errors η_i made in assuming the f model to represent the v data are

$$\eta_i \;=\; v_i \;-\; f(u_i; q_1, \ldots, q_n), \qquad i = 1, \ldots, m, \qquad (B1)$$

and define collectively the vector error η for f. The sum of squares of these errors η_i defines the F function, which is given by

$$\begin{aligned} F \;&=\; F(q) \\ &=\; \sum_{i=1}^{m} \eta_i^2 \\ &=\; \sum_{i=1}^{m} \left[v_i - f(u_i; q_1, \ldots, q_n) \right]^2. \end{aligned} \qquad (B2)$$

In terms of the fitting parameters and the formulation of the fitting process, the F function has to be minimized with respect to q to obtain a measurement-model *least-squares* fit. The vector of parameters q, which make the fitting function nonlinear, might be bounded or constrained, but for the scope of the work presented in this study, they are considered to be free and independent.

The IDL least-squares fitting routine (`non-lin-lsq.pro`) was executed by iteratively applying a gradient-expansion algorithm. The routine returned the converged *best* fitted parameter set $\hat{q}$ minimizing F, together with the Jacobian matrix J_η of the errors η with respect to the q set evaluated at $q = \hat{q}$. The Hessian matrix H_F, of the sum of squares F of the error η, can be written in a approximated form as $H_F \simeq 2 J_\eta^T J_\eta$ (where J_η^T is the transpose of J_η), while the inverse of H_F is the so-called *variance-covariance* matrix C_F of the errors η with respect to the q set of parameters.

Let χ^2_F be the sum of squares F, evaluated at $q = \hat{q}$ and divided by the degrees of freedom $m - n$. After matrix inversion on the $J_\eta^T J_\eta$ matrix product, thus deriving the elements of the variance-covariance matrix, and after evaluating such elements at $q = \hat{q}$, thus obtaining a matrix C_F, an unbiased estimator of the variance of f, at any value $u_i = \dot{u}$ of the independent variable, is given by

$$\mathrm{var}[f(\dot{u};\hat{q})] \;=\; 2\,\chi^2_f \sum_{j,k=1}^{n} \left\{ \hat{C}_F \right\}_{jk} \left. \widehat{\frac{\partial f}{\partial q_j}} \right|_{\dot{u}} \left. \widehat{\frac{\partial f}{\partial q_k}} \right|_{\dot{u}}, \qquad (B3)$$

where the $\widehat{\ }$ symbol indicates determination of the partial derivative at $q = \hat{q}$. Taking the square root of ($B3$) yields $\sigma_f(\dot{u};\hat{q})$, or the standard deviation on the fitted function, determined at $q = \hat{q}$ and $u_i = \dot{u}$.

If $\breve{q}$ is the *true* parameter set, then with $100(1 - \vartheta)$ confidence the real radiometric value at point $\dot{u}$ is contained in a confidence interval $I_f(\dot{u};\breve{q})$, centered around the fitted function value $f(\dot{u};\hat{q})$, and given by

$$I_f(\dot{u};\breve{q}) \;=\; f(\dot{u};\hat{q}) \;\pm\; t_\kappa \sigma_f(\dot{u};\hat{q}), \qquad (B4)$$

where $\vartheta \in [0,1]$ is an arbitrary value chosen to obtain the required percent confidence level $100(1-\vartheta)$, and t_κ is the $100\vartheta/2$ percentage point of the single-tailed t-distribution with $m-n$ degrees of freedom, e.g., the tabulated values in Draper and Smith (1981).

Appendix C

Nonlinear Confidence Bands

The sum of the squares function F is a function of the fit parameter elements only, and in the parameter space this function can be represented by the contours of a surface (Draper and Smith 1981). If the model is linear with respect to the parameters, the surface contours would be ellipsoids and have a single local minimum, at the location defined by the least-squares estimator. If the model is nonlinear, the contours are not ellipsoids, but tend to be irregular, and more than one local minima may be found.

Nonlinear curve fitting to experimental data tends, therefore, to suffer from ill-conditioning (multiple local minima may be found in the iterative fitting procedure, depending on the chosen initial point). The accepted way to deal with this problem is to consider the corresponding linearized form of the nonlinear model (the one obtained by approximating the nonlinear model with a Taylor expansion, which is linear with respect to the parameters) in the vicinity of the solution minimizing the sum of squares.

From the linearized model, the contour providing the exact ellipsoidal boundary at the required confidence level is generated, and then labeled as being an approximate confidence boundary in the nonlinear case (Draper and Smith 1981). It is important to note the contour determined in this fashion will be a correct confidence contour in the nonlinear case (and will not be elliptical in general), and it is only the probability level that is approximate.

Glossary

3-D	Three-Dimensional
A/D	Analog-to-Digital
AAOT	*Acqua Alta* Oceanographic Tower
AOPs	Apparent Optical Properties
CNR	*Consiglio Nazionale delle Ricerche*
CoASTS	Coastal Atmosphere and Sea Time-Series
CTD	Conductivity, Temperature, and Depth
GMT	Greenwich Mean Time
GSFC	Goddard Space Flight Center
IDL	Interactive Data Language
IOPs	Inherent Optical Properties
ISDGM	*Istituto per lo Studio della Dinamica delle Grandi Masse*
LDDS	Long Distance Deployment System
LoCNESS	Low Cost NASA Environmental Sampling System
MC	Monte Carlo
miniNESS	miniature NASA Environmental Sampling System
MVDS	Multichannel Visible Detector System
NASA	National Aeronautics and Space Administration
OCI	Ocean Color Irradiance
OCR	Ocean Color Radiance
PRE	Percent Relative Error
SDY	Sequential Day of the Year
SeaFALLS	SeaWiFS Free-Falling Advanced Light Level Sensor
SeaWiFS	Sea-viewing Wide Field-of-view Sensor
S/N	Serial Number
SPMR	Satlantic SeaWiFS Profiling Multichannel Radiometer
UPD	Unbiased Percent Difference
WETLabs	Western Environmental Technology Laboratories
WiSPER	Wire-Stabilized Profiling Environmental Radiometer

Symbols

$a(\lambda)$	Spectral absorption coefficient.
$a_p(\lambda)$	Spectral absorption coefficient of particulate matter.
$\hat{a}_{t-w}^{ST}$	The AC-9 absorption coefficient for particles and dissolved organic matter, corrected for salinity and temperature effects.
$\breve{a}_{t-w}^{ST}$	The AC-9 correction term for the absorption coefficient.
$a_w(\lambda)$	Spectral absorption coefficient of pure seawater.
$a_y(\lambda)$	Spectral absorption coefficient of dissolved organic matter.
$c(\lambda)$	Spectral beam attenuation coefficient.
C	Superscript for absolute geophysical units.
C_a	Chlorophyll a concentration.
C_F	The covariance matrix of vector errors η.
$c_p(\lambda)$	Spectral beam attenuation coefficient of particulate matter.
C_{TSM}	Total Suspended Matter concentration.
$c_w(\lambda)$	Spectral beam attenuation coefficient of pure seawater.
c_{xi}	Calibration coefficients with $i = 0, \ldots, 2$.
c_{yi}	Calibration coefficients with $i = 0, \ldots, 2$.
$c_y(\lambda)$	Spectral beam attenuation coefficient of dissolved organic matter (yellow substance).
$\hat{c}_{t-w}^{ST}$	The AC-9 beam attenuation coefficient for particles and dissolved organic matter, corrected for salinity and temperature effects.
$E_d(\lambda)$	Spectral downward irradiance.
$E_d(0^+, \lambda)$	Spectral above-water (solar) downward irradiance.
$E'_d(\lambda)$	Normalized downward irradiance.
$E_i(\lambda)$	Spectral indirect (diffuse) irradiance.
$E_u(\lambda)$	Spectral upward irradiance.
f	A vector function.
F	A function defined by the sum of squares of η_i.
H_F	Hessein matrix of function F.
I	Superscript for the immersion coefficients.
I_f	The confidence interval.
J_η	The Jacobian matrix of vector error η.
J_η^T	The transpose of J_η.
$K_d(\lambda)$	Spectral diffuse attenuation coefficient for $E_d(\lambda)$.

$L_u(\lambda)$ Spectral upwelling radiance.
$L'_u(\lambda)$ Spectral normalized upwelling radiance.
$L_W^F(\lambda)$ The spectral water-leaving radiance derived from LoCNESS and SeaFALLS measurements.
$L_W^M(\lambda)$ The spectral water-leaving radiance derived from miniNESS measurements.
m The number of observations.
n The number of parameters.
O The superscript for offset data.
p Pressure.
p^S A scale factor for the pressure gauge.
$\mathfrak{P}$ A shadow-free quantity.
$\mathfrak{P}'$ A far-field quasi-unperturbed quantity.
$\breve{\mathfrak{P}}$ A shadow-perturbed quantity.
q A vector of n parameters.
$\hat{q}$ Best fitted parameter set minimizing function F.
$\breve{q}$ True parameter set.
q_i The q component for observation i.
r_d The ratio of the diffuse to direct downward irradiance.
$R_{\rm rs}(\lambda)$ Spectral remote sensing reflectance.
S The superscript for scale factors.
t Time.
t_0 The starting time.
t_i Time for depth z_i.
u The vector of m independent variables.
u_i The u component for observation i.
v The vector of m dependent variables.
v_i v component for observation i.
W Wind speed.
x The distance from the AAOT tower.
X An arbitrary x quantity.
y Horizontal displacement.
Y An arbitrary y quantity.
z Depth.
z_i Binning depth.
α Positive parameter of the ω function.
β Positive parameter of the ω function.
γ Positive parameter of the ω function.
$\varepsilon_{\mathfrak{P}}$ Percent relative error with respect to $\mathfrak{P}$.
$\varepsilon'_{\mathfrak{P}}$ Percent relative error with respect to $\mathfrak{P}'$.
η The vector error for the vector function f.
η_i The η component for observation i.
θ Solar zenith angle.
ϑ An arbitrary value within the 0–1 interval.
t_κ $100\vartheta/2$ percentage points of the t-distribution with $m-n$ degrees of freedom.
λ Wavelength.
λ_0 A reference wavelength.
σ Standard deviation.
σ_f The standard deviation of the fitted function.
$\tau_A(\lambda)$ The aerosol optical depth.
$\tau_O(\lambda)$ The ozone optical depth.
$\tau_R(\lambda)$ The (Rayleigh) molecular optical depth.
ϕ Solar azimuth angle.
φ The vertical tilt.
φ_x The x-axis component of the vertical tilt.
φ_y The y-axis component of the vertical tilt.
χ^2 The statistic quantifying the goodness of the fit.
χ^2_F The sum of squares F.
$\bar{\psi}$ Unbiased percent difference.
ω Monomolecular function.

References

Aiken, J., D.G. Cummings, S.W. Gibb, N.W. Rees, R. Woodd-Walker, E.M.S. Woodward, J. Woolfenden, S.B. Hooker, J-F. Berthon, C.D. Dempsey, D.J. Suggett, P. Wood, C. Donlon, N. González-Benítez, I. Huskin, M. Quevedo, R. Barciela-Fernandez, C. de Vargas, and C. McKee, 1998: AMT-5 Cruise Report. *NASA Tech. Memo. 1998–206892, Vol. 2,* S.B. Hooker and E.R. Firestone, Eds., NASA Goddard Space Flight Center, Greenbelt, Maryland, 113 pp.

Berthon, J-F., G. Zibordi, and S.B. Hooker, 1999: Marine optical measurements of a mucilage event in the Northern Adriatic Sea. *Limnol. Oceanogr.,* **45,** 322–327.

——, ——, J.P. Doyle, D.W. van der Linde, S. Grossi, and C. Targa, 2002: Coastal Atmosphere and Sea Time Series (CoASTS), Part 2: Data Analysis. *NASA Tech. Memo. 2002-206892, Vol. 20,* S.B. Hooker and E.R. Firestone, Eds., NASA Goddard Space Flight Center, Greenbelt, Maryland, 25 pp.

Doyle, J.P., and G. Zibordi, 2002: Optical propagation within a 3-D shadowed atmosphere–ocean field: Application to large deployment structures. *Appl. Opt.,* **42,** 4,283–4,306.

Draper, N.R., and H. Smith, 1981: *Applied Regression Analysis.* Wiley, New York, 709 pp.

Hooker, S.B., G. Zibordi, G. Lazin, and S. McLean, 1999: The SeaBOARR-98 Field Campaign. *NASA Tech. Memo. 1999–206892, Vol. 3,* S.B. Hooker and E.R. Firestone, Eds., NASA Goddard Space Flight Center, Greenbelt, Maryland, 40 pp.

——, and S. Maritorena, 2000: An evaluation of oceanographic radiometers and deployment methodologies. *J. Atmos. Ocean. Technol.,* **17,** 811–830.

——, and C.R. McClain, 2000: A comprehensive plan for the calibration and validation of SeaWiFS data. *Prog. Oceanogr.,* **45,** 427–465.

——, S. McLean, J. Sherman, M. Small, G. Lazin, G. Zibordi, and J.W. Brown, 2002: The Seventh SeaWiFS Intercalibration Round-Robin Experiment (SIRREX-7), March 1999. *NASA Tech. Memo. 2002–206892, Vol. 17,* S.B. Hooker and E.R. Firestone, Eds., NASA Goddard Space Flight Center, Greenbelt, Maryland, 69 pp.

——, G. Zibordi, J-F. Berthon, D. D'Alimonte, D. van der Linde, and J.W. Brown, 2003: Tower-Perturbation Measurements in Above-Water Radiometry. *NASA Tech. Memo. 2003–206892, Vol. 23,* S.B. Hooker and E.R. Firestone, Eds., NASA Goddard Space Flight Center, Greenbelt, Maryland, 35 pp.

Gordon, H.R., 1985: Ship perturbation of irradiance measurements at sea. 1: Monte Carlo simulations. *Appl. Opt.,* **24,** 4,172–4,182.

——, and K. Ding, 1992: Self-shading of in-water optical instruments. *Limnol. Oceanogr.,* **37,** 491–500.

Marquardt, D.W., 1963: An algorithm for least squares estimation of nonlinear parameters. *J. Soc. Ind. Appl. Math.,* **2,** 431–441.

Molin, D., E. Guidoboni, and A. Lodovisi, 1992: "Mucilage and the phenomenon of algae in the history of the Adriatic: Periodization and the anthropic context (17th–20th centuries)." In: Wollenweider, R.A., R. Marchetti, R. Viviani, Eds., Marine Coastal Eutrophication. Proceedings of an International Conference, Bologna, Italy, 21–24 March
1990. *Sci. Total Environ., Suppl.,* 511–524.

Morel, A., and L. Prieur, 1977: Analysis of variations in ocean color. *Limnol. Oceanogr.,* **22,** 709–722.

Pope, R.M., and E.S. Fry, 1997: Absorption spectrum (380–700 nm) of pure water, II. Integrating cavity measurements, *Appl. Opt.,* **36,** 8,710–8,723.

Spanier, J., and E.M. Gelbard, 1969: *Monte Carlo Principles and Neutron Transport Problems.* Addison-Wesley, Reading, Massachusetts, 234 pp.

WETLabs, 2002: *AC-9 Protocol Document.* [World Wide Web page.] From URL: `http://www.wetlabs.com/Products/pub/ac9/` WETLabs, Inc., Philomath, Oregon.

World Meteorological Organization, 1983: *Guide to the Meteorological Instruments and Methods of Observation,* WMO–N.8, 517 pp.

Zaneveld, J.R., J.C. Kitchen, and C. Moore, 1994: The scattering error coefficient of reflective absorption measurements. *Proc. SPIE, Ocean Optics XII,* **2258,** 44–54.

Zibordi, G., and M. Ferrari, 1995: Instrument self-shading in underwater optical measurements: Experimental data. *Appl. Opt.,* **34,** 2,750–2,754.

——, J.P. Doyle, and S.B. Hooker, 1999: Offshore Tower Shading Effects on In-Water Optical Measurements. *J. Atmos. Ocean. Tech.,* **16,** 1,767–1,779.

Zibordi, G., J-F. Berthon, J.P. Doyle, S. Grossi, D. van der Linde, C. Targa, and L. Alberotanza 2002: Coastal Atmosphere and Sea Time Series (CoASTS), Part 1: A Tower-Based Long-Term Measurement Program. *NASA Tech. Memo. 2002–206892, Vol. 19,* S.B. Hooker and E.R. Firestone, Eds., NASA Goddard Space Flight Center, Greenbelt, Maryland, 29 pp.

The SeaWiFS Postlaunch Technical Report Series

Vol. 1

Johnson, B.C., J.B. Fowler, and C.L. Cromer, 1998: The SeaWiFS Transfer Radiometer (SXR). *NASA Tech. Memo. 1998–206892, Vol. 1,* S.B. Hooker and E.R. Firestone, Eds., NASA Goddard Space Flight Center, Greenbelt, Maryland, 58 pp.

Vol. 2

Aiken, J., D.G. Cummings, S.W. Gibb, N.W. Rees, R. Woodd-Walker, E.M.S. Woodward, J. Woolfenden, S.B. Hooker, J-F. Berthon, C.D. Dempsey, D.J. Suggett, P. Wood, C. Donlon, N. González-Benítez, I. Huskin, M. Quevedo, R. Barciela-Fernandez, C. de Vargas, and C. McKee, 1998: AMT-5 Cruise Report. *NASA Tech. Memo. 1998–206892, Vol. 2,* S.B. Hooker and E.R. Firestone, Eds., NASA Goddard Space Flight Center, Greenbelt, Maryland, 113 pp.

Vol. 3

Hooker, S.B., G. Zibordi, G. Lazin, and S. McLean, 1999: The SeaBOARR-98 Field Campaign. *NASA Tech. Memo. 1999–206892, Vol. 3,* S.B. Hooker and E.R. Firestone, Eds., NASA Goddard Space Flight Center, Greenbelt, Maryland, 40 pp.

Vol. 4

Johnson, B.C., E.A. Early, R.E. Eplee, Jr., R.A. Barnes, and R.T. Caffrey, 1999: The 1997 Prelaunch Radiometric Calibration of SeaWiFS. *NASA Tech. Memo. 1999–206892, Vol. 4,* S.B. Hooker and E.R. Firestone, Eds., NASA Goddard Space Flight Center, Greenbelt, Maryland, 51 pp.

Vol. 5

Barnes, R.A., R.E. Eplee, Jr., S.F. Biggar, K.J. Thome, E.F. Zalewski, P.N. Slater, and A.W. Holmes 1999: The SeaWiFS Solar Radiation-Based Calibration and the Transfer-to-Orbit Experiment. *NASA Tech. Memo. 1999–206892, Vol. 5,* S.B. Hooker and E.R. Firestone, Eds., NASA Goddard Space Flight Center, 28 pp.

Vol. 6

Firestone, E.R., and S.B. Hooker, 2000: SeaWiFS Postlaunch Technical Report Series Cumulative Index: Volumes 1–5. *NASA Tech. Memo. 2000–206892, Vol. 6,* S.B. Hooker and E.R. Firestone, Eds., NASA Goddard Space Flight Center, Greenbelt, Maryland, 14 pp.

Vol. 7

Johnson, B.C., H.W. Yoon, S.S. Bruce, P-S. Shaw, A. Thompson, S.B. Hooker, R.E. Eplee, Jr., R.A. Barnes, S. Maritorena, and J.L. Mueller, 1999: The Fifth SeaWiFS Intercalibration Round-Robin Experiment (SIRREX-5), July 1996. *NASA Tech. Memo. 1999–206892, Vol. 7,* S.B. Hooker and E.R. Firestone, Eds., NASA Goddard Space Flight Center, 75 pp.

Vol. 8

Hooker, S.B., and G. Lazin, 2000: The SeaBOARR-99 Field Campaign. *NASA Tech. Memo. 2000–206892, Vol. 8,* S.B. Hooker and E.R. Firestone, Eds., NASA Goddard Space Flight Center, 46 pp.

Vol. 9

McClain, C.R., E.J. Ainsworth, R.A. Barnes, R.E. Eplee, Jr., F.S. Patt, W.D. Robinson, M. Wang, and S.W. Bailey, 2000: SeaWiFS Postlaunch Calibration and Validation Analyses, Part 1. *NASA Tech. Memo. 2000–206892, Vol. 9,* S.B. Hooker and E.R. Firestone, Eds., NASA Goddard Space Flight Center, 82 pp.

Vol. 10

McClain, C.R., R.A. Barnes, R.E. Eplee, Jr., B.A. Franz, N.C. Hsu, F.S. Patt, C.M. Pietras, W.D. Robinson, B.D. Schieber, G.M. Schmidt, M. Wang, S.W. Bailey, and P.J. Werdell, 2000: SeaWiFS Postlaunch Calibration and Validation Analyses, Part 2. *NASA Tech. Memo. 2000–206892, Vol. 10,* S.B. Hooker and E.R. Firestone, Eds., NASA Goddard Space Flight Center, 57 pp.

Vol. 11

O'Reilly, J.E., S. Maritorena, M.C. O'Brien, D.A. Siegel, D. Toole, D. Menzies, R.C. Smith, J.L. Mueller, B.G. Mitchell, M. Kahru, F.P. Chavez, P. Strutton, G.F. Cota, S.B. Hooker, C.R. McClain, K.L. Carder, F. Müller-Karger, L. Harding, A. Magnuson, D. Phinney, G.F. Moore, J. Aiken, K.R. Arrigo, R. Letelier, and M. Culver 2000: SeaWiFS Postlaunch Calibration and Validation Analyses, Part 3. *NASA Tech. Memo. 2000–206892, Vol. 11,* S.B. Hooker and E.R. Firestone, Eds., NASA Goddard Space Flight Center, 49 pp.

Vol. 12

Firestone, E.R., and S.B. Hooker, 2000: SeaWiFS Postlaunch Technical Report Series Cumulative Index: Volumes 1–11. *NASA Tech. Memo. 2000–206892, Vol. 12,* S.B. Hooker and E.R. Firestone, Eds., NASA Goddard Space Flight Center, Greenbelt, Maryland, 24 pp.

Vol. 13

Hooker, S.B., G. Zibordi, J-F. Berthon, S.W. Bailey, and C.M. Pietras, 2000: The SeaWiFS Photometer Revision for Incident Surface Measurement (SeaPRISM) Field Commissioning. *NASA Tech. Memo. 2000–206892, Vol. 13,* S.B. Hooker and E.R. Firestone, Eds., NASA Goddard Space Flight Center, Greenbelt, Maryland, 24 pp.

Vol. 14

Hooker, S.B., H. Claustre, J. Ras, L. Van Heukelem, J-F. Berthon, C. Targa, D. van der Linde, R. Barlow, and H. Sessions, 2000: The First SeaWiFS HPLC Analysis Round-Robin Experiment (SeaHARRE-1). *NASA Tech. Memo. 2000–206892, Vol. 14,* S.B. Hooker and E.R. Firestone, Eds., NASA Goddard Space Flight Center, Greenbelt, Maryland, 42 pp.

Vol. 15

Hooker, S.B., G. Zibordi, J-F. Berthon, D. D'Alimonte, S. Maritorena, S. McLean, and J. Sildam, 2001: Results of the Second SeaWiFS Data Analysis Round Robin, March 2000 (DARR-00). *NASA Tech. Memo. 2001–206892, Vol. 15,* S.B. Hooker and E.R. Firestone, Eds., NASA Goddard Space Flight Center, Greenbelt, Maryland, 71 pp.

Vol. 16

Patt, F.S., 2002: Navigation Algorithms for the SeaWiFS Mission. *NASA Tech. Memo. 2002–206892, Vol. 16,* S.B. Hooker and E.R. Firestone, Eds., NASA Goddard Space Flight Center, Greenbelt, Maryland, 17 pp.

Vol. 17

Hooker, S.B., S. McLean, J. Sherman, M. Small, G. Lazin, G. Zibordi, and J.W. Brown, 2002: The Seventh SeaWiFS Intercalibration Round-Robin Experiment (SIRREX-7), March 1999. *NASA Tech. Memo. 2002–206892, Vol. 17,* S.B. Hooker and E.R. Firestone, Eds., NASA Goddard Space Flight Center, Greenbelt, Maryland, 69 pp.

Vol. 18

Firestone, E.R., and S.B. Hooker, 2003: SeaWiFS Postlaunch Technical Report Series Cumulative Index: Volumes 1–17. *NASA Tech. Memo. 2003–206892, Vol. 18,* S.B. Hooker and E.R. Firestone, Eds., NASA Goddard Space Flight Center, Greenbelt, Maryland, 28 pp.

Vol. 19

Zibordi, G., J-F. Berthon, J.P. Doyle, S. Grossi, D. van der Linde, C. Targa, and L. Alberotanza 2002: Coastal Atmosphere and Sea Time Series (CoASTS), Part 1: A Tower-Based Long-Term Measurement Program. *NASA Tech. Memo. 2002–206892, Vol. 19,* S.B. Hooker and E.R. Firestone, Eds., NASA Goddard Space Flight Center, Greenbelt, Maryland, 29 pp.

Vol. 20

Berthon, J-F., G. Zibordi, J.P. Doyle, S. Grossi, D. van der Linde, and C. Targa, 2002: Coastal Atmosphere and Sea Time Series (CoASTS), Part 2: Data Analysis. *NASA Tech. Memo. 2002–206892, Vol. 20,* S.B. Hooker and E.R. Firestone, Eds., NASA Goddard Space Flight Center, Greenbelt, Maryland, 25 pp.

Vol. 21

Zibordi, G., D. D'Alimonte, D. van der Linde, J-F. Berthon, S.B. Hooker, J.L. Mueller, G. Lazin, and S. McLean, 2002: The Eighth SeaWiFS Intercalibration Round-Robin Experiment (SIRREX-8), September–December 2001. *NASA Tech. Memo. 2002–206892, Vol. 21,* S.B. Hooker and E.R. Firestone, Eds., NASA Goddard Space Flight Center, Greenbelt, Maryland, 39 pp.

Vol. 22

Patt, F.S., R.A. Barnes, R.E. Eplee, Jr., B.A. Franz, W.D. Robinson, G.C. Feldman, S.W. Bailey J. Gales, P.J. Werdell, M. Wang, R. Frouin, R.P. Stumpf, R.A. Arnone, R.W. Gould, Jr., P.M. Martinolich, V. Ransibrahmanakul, J.E. O'Reilly, and J.A. Yoder, 2003: Algorithm Updates for the Fourth SeaWiFS Data Reprocessing, *NASA Tech. Memo. 2003–206892, Vol. 22,* S.B. Hooker and E.R. Firestone, Eds., NASA Goddard Space Flight Center, Greenbelt, Maryland, 74 pp.

Vol. 23

Hooker, S.B., G. Zibordi, J-F. Berthon, D. D'Alimonte, D. van der Linde, and J.W. Brown, 2003: Tower-Perturbation Measurements in Above-Water Radiometry. *NASA Tech. Memo. 2003–206892, Vol. 23,* S.B. Hooker and E.R. Firestone, Eds., NASA Goddard Space Flight Center, Greenbelt, Maryland, 35 pp.

Vol. 24

Firestone, E.R., and S.B. Hooker, 2003: SeaWiFS Postlaunch Technical Report Series Cumulative Index: Volumes 1–23. *NASA Tech. Memo. 2003–206892, Vol. 24,* S.B. Hooker and E.R. Firestone, Eds., NASA Goddard Space Flight Center, Greenbelt, Maryland, (in prep.).

Vol. 25

Doyle, J.P., S.B. Hooker, G. Zibordi, and D. van der Linde, 2003: Validation of an In-Water, Tower-Shading Correction Scheme. *NASA Tech. Memo. 2003–206892, Vol. 25,* S.B. Hooker and E.R. Firestone, Eds., NASA Goddard Space Flight Center, Greenbelt, Maryland, 32 pp.

REPORT DOCUMENTATION PAGE

Form Approved
OMB No. 0704-0188

1. AGENCY USE ONLY *(Leave blank)*	2. REPORT DATE	3. REPORT TYPE AND DATES COVERED
	June 2003	Technical Memorandum

4. TITLE AND SUBTITLE
SeaWiFS Postlaunch Technical Report Series
Volume 25: Validation of an In-Water, Tower-Shading Correction Scheme

5. FUNDING NUMBERS
970.2

6. AUTHORS
J.P. Doyle, S.B. Hooker, G. Zibordi, and D. van der Linde

Series Editors: Stanford B. Hooker and Elaine R. Firestone

7. PERFORMING ORGANIZATION NAME(S) AND ADDRESS(ES)
Laboratory for Hydrospheric Processes
Goddard Space Flight Center
Greenbelt, Maryland 20771

8. PERFORMING ORGANIZATION REPORT NUMBER
2003-01912-0

9. SPONSORING/MONITORING AGENCY NAME(S) AND ADDRESS(ES)
National Aeronautics and Space Administration
Washington, D.C. 20546–0001

10. SPONSORING/MONITORING AGENCY REPORT NUMBER
TM—2003–206892, Vol. 25

11. SUPPLEMENTARY NOTES
E.R. Firestone: Science Applications International Corporation, Beltsville, Maryland; J.P. Doyle: JRC/Space Applications Institute, Ispra, Italy; G. Zibordi and D. van der Linde: JRC/Institute for Environment and Sustainability, Ispra, Italy

12a. DISTRIBUTION/AVAILABILITY STATEMENT
Unclassified–Unlimited
Subject Category 48
Report is available from the Center for AeroSpace Information (CASI),
7121 Standard Drive, Hanover, MD 21076–1320; (301)621-0390

12b. DISTRIBUTION CODE

13. ABSTRACT *(Maximum 200 words)*

Large offshore structures used for the deployment of optical instruments can significantly perturb the intensity of the light field surrounding the optical measurement point, where different portions of the visible spectrum are subject to different shadowing effects. These effects degrade the quality of the acquired optical data and can reduce the accuracy of several derived quantities, such as those obtained by applying bio-optical algorithms directly to the shadow-perturbed data. As a result, optical remote sensing calibration and validation studies can be impaired if shadowing artifacts are not fully accounted for. In this work, the general in-water shadowing problem is examined for a particular case study. Backward Monte Carlo (MC) radiativetransfer computations—performed in a vertically stratified, horizontally inhomogeneous, and realistic ocean–atmosphere system—are shown to accurately simulate the shadow-induced relative percent errors affecting the radiance and irradiance data profiles acquired close to an oceanographic tower. Multiparameter optical data processing has provided adequate representation of experimental uncertainties allowing consistent comparison with simulations. The more detailed simulations at the subsurface depth appear to be essentially equivalent to those obtained assuming a simplified ocean--atmosphere system, except in highly stratified waters. MC computations performed in the simplified system can be assumed, therefore, to accurately simulate the optical measurements conducted under more complex sampling conditions (i.e., within waters presenting moderate stratification at most). A previously reported correction scheme, based on the simplified MC simulations, and developed for subsurface shadow-removal processing of in-water optical data taken close to the investigated oceanographic tower, is then validated adequately under most experimental conditions. It appears feasible to generalize the present tower-specific approach to solve other optical sensor shadowing problems pertaining to differently shaped deployment platforms, and also including surrounding structures and instrument casings.

14. SUBJECT TERMS
SeaWiFS, Oceanography, Tower-Shading, Above-Water, Correction Scheme, Radiometry, In-Water, Data Analysis Methods, In Situ Sampling

15. NUMBER OF PAGES
32

16. PRICE CODE

17. SECURITY CLASSIFICATION OF REPORT	18. SECURITY CLASSIFICATION OF THIS PAGE	19. SECURITY CLASSIFICATION OF ABSTRACT	20. LIMITATION OF ABSTRACT
Unclassified	Unclassified	Unclassified	Unlimited